2011

Novel transparent conductive materials: understanding and prediction

Yaou Song

Department:

NOVEL TRANSPARENT CONDUCTIVE MATERIALS:

UNDERSTANDING AND PREDICTION

by

YAOU SONG

A THESIS

Presented to the Faculty of the Graduate School of the

MISSOURI UNIVERSITY OF SCIENCE AND TECHNOLOGY

In Partial Fulfillment of the Requirements for the Degree

MASTER OF SCIENCE IN PHYSICS

2011

Approved by

Julia E. Medvedeva
Paul Parris
Yew San Hor

ABSTRACT

Transparent conductive oxides (TCOs) such as doped In_2O_3, ZnO, SnO_2 or CdO are highly attractive due to their special properties, which are electrical conductivity and optical transparency. The lack of complete understanding of the fundamentals behind this unique phenomena and rapidly increasing commercial demand draw a lot of interest in investigating this kind of materials. More efficient, environmentally friendly and less expensive transparent conductive materials are needed for a variety of applications, and a general understanding of the origins of the unusual behavior would help further search for potential transparent conductive (TC) candidates.

Understanding the basic properties of conventional TCOs theory and predicting new TC candidates are the two main goals of this study. To achieve these goals, several classes of materials including conventional TCOs and other metal oxides, nitrides, selenides, sulfides, fluorides and a few others were investigated by using first-principles electronic band structure simulations. Compounds with same-group next-period cations or anions are studied. For example, vertical chains of compounds $Al_2O_3 \rightarrow Ga_2O_3 \rightarrow In_2O_3 \rightarrow Tl_2O_3$, and $In_2O_3 \rightarrow In_2S_3 \rightarrow In_2Se_3 \rightarrow In_2Te_3$, were systematically considered. The results comprise electronic band structure, band gap, density of states, electron effective mass and holes effective mass. The calculated materials were separated into different groups based on the location of the cation or anion in the periodic table, i.e., on its electronic configuration or atomic weight, and comparisons were carried out within the same group. The differences among the compounds in the same series are discussed in details based on the calculated results.

ACKNOWLEDGMENTS

So many have encouraged me and supported me along this journey, and so many to express my deep and sincere gratitude to at the beginning of this thesis. My first and most earnest acknowledgment goes to my advisor, Professor Julia E. Medvedeva, for her confidence in me when she welcomed me into her research group soon after I came to MS&T. Her natural interests in research, sharp interpretation of puzzling problems, and everlasting enthusiasm serve as the best mentor one could ask for. Her tireless support and guidance throughout these years have forged an indispensable part into this thesis. I have learnt from her to be thorough, responsible, hard-working, and to always look on the bright side in times of difficulty. I owe this work to her in countless ways and this appreciation shall accompany me in the many years to come.

In that same vein, many thanks go to the committee members: Dr. Paul Parris, Dr. Yew San Hor for their time and efforts to go through this thesis and offer me this opportunity to defend it in front of them. My gratitude is also extended to the other members of Dr. Medvedeva's group, Altybek Murat, for his help and cooperation. I would also like to take this opportunity to make a special acknowledgment to my friends in the physics department. The friendship has made these years very joyful. Their enthusiasm and passion for research accompanied me throughout this journey.

Special and personal thanks go to my parents and my lovely siblings for their tremendous support and love for going through these years with me. They believed in me and my ability to achieve something even when I myself have doubt about it. Their unwavering faith and confidence in me and my abilities have shaped me to be the person I am today.

TABLE OF CONTENTS

LIST OF ILLUSTRATIONS

LIST OF TABLES

1. INTRODUCTION

1.1. BACKGROUND

Transparent conductive oxides (TCOs) belong to a class of materials that are unique in the sense that two seemingly contradictory properties - electrical conductivity and optical transparency - coexist in the same material. This special property makes TCOs remarkable materials used in products for commercial purposes. Ever since Badeker discovered in 1907 that he could render a thin Cadmium film transparent while maintaining reasonable conductivity simply by oxidizing the metal to produce CdO [1], the field of transparent conducting oxides has developed. Although, the first reports date back to early 1900s, it was not until the last few decades that these materials were employed in commercial products.[2] The first widespread use was as transparent electrical heaters for aircraft windshield de-icing during the World War 2.[3] Since then, the applications and technological possibilities for TCOs have continued to increase. TCOs have attracted increasingly considerable attention in recent years; the MRS Bulletin devoted an issue to the topic in August of 2000, and two books have been published in 2010. [4, 5]

Recent renewed interest in research on TCOs is mainly due to an exponential rise in the applications using TCO materials.[6] With the advent of flexible displays, high definition TVs (HDTVs), flat panel displays (FPDs) and several hand-held and smart devices, the demand for TCOs has also increased several fold.[7] Another important application for the TCOs is energy efficient windows, which is gaining significance in the global regions with cold or moderate climates.[8] However, the most important application in the present context is that of transparent electrodes for light emitting diodes

(LEDs) and for photovoltaic (PV) cells.[9] With an ever deepening energy crisis, the demand for alternative and cost-effective energy sources is increasing. There is also a need to improve the efficiency of solid state lighting devices, in order to address the issue of energy conservation.[9] Although rapid progress is being made in increasing efficiency of the above-mentioned solid state devices through breakthrough results in synthesis of photoactive materials and novel device structures, the research in the field of TCOs has been relatively slow paced.[7,9] Soon, the TCO properties will be the limiting factor in the development of PVs and the solid state lighting devices.[10] Therefore, there is a considerable interest in developing TCOs with improved properties. On the other hand, it is clear that there is no one TCO that is best for all applications. Fluorine-doped tin oxide is the most widely used TCO, while tin-doped indium oxide (ITO) remains preferred for flat-panel displays. [11] Zinc oxide has potential for use in more efficient and less expensive solar cells. [12] All of these commonly used transparent conducting materials and their production methods have advantages and disadvantages that must be carefully weighed for each application.

Thus, in the last few years, there has been an increasing realization that the conventional TCO material set of substitutionally doped crystalline SnO_2, ZnO and In_2O_3 materials are no longer sufficient to meet the needs for a wide range of TCO applications. Also, the shortages of currently used TCOs have become a big concern. For instance, currently, indium tin oxide (ITO) is the most widely used material for many TCO applications. With the steady rise in demand for the applications mentioned earlier, it seems to be difficult to meet the supply requirements because of the rapidly diminishing supply of In. In the recent years the production of In has dropped by about 12%, and

increasing the production is itself a topic of intense research. [13] The primary reason for the limited availability of In is that it is produced as a by-product of Zn, Sn and Pb production. The concentration of In in earth's crust is rather low (0.1 ppb), which prohibits direct mining of this element. [14] Thus, increasing the output of In would require drastic improvement in the extraction processes and equipment. This directly translates into addition of cost to the present high prices of In. Currently, 4N (99.99) purity In costs $2000/kg, which is ten times higher as compared to the price in 2003. The price is even higher for a higher grade In and its alloys. In 2005 – 06, 70% of the In produced globally was used in the form of ITO coating for various TCO applications.[15] A large fraction of the remaining In is mostly used as an electronic grade material for semiconductor and electrical components. One such compound is InP, which is being explored for the next generation transistors in order to keep up with the Moore's law for semiconductor roadway.[16] Another application where In could play an important role is CuInGaSe (CIGS) based photovoltaic devices, especially in the light of the fact that it is becoming increasingly difficult to keep up the production of solar-grade silicon.[17] Although the demand for In based compound semiconductors has been steady over the past few years, it is predicted to pick up in the future. Soon, the manufacturers of In based compound semiconductor devices will be competing with the ITO producers for a larger share of In. The annual consumption of TCO coated windows (primarily for low-e coatings) in the United States is 7.3×10^7 m^2 and translates into a billion dollar industry. Similarly, the demand for FPD has grown over $27 billion over the past few years and is expected to increase even further.[8] The automotive sector is another huge market for the TCO coatings and can be directly associated with the demand for the commercial

vehicles. Thus, substituting ITO with a more economical TCO material would save a large amount of material related costs of the TCO based products. Moreover, a stable supply of In would also assure for the semiconductor and optoelectronic applications.

In addition to the high cost of In, ITO is also brittle, suffers from poor chemical stability in hydrogen atmospheres and exhibits relatively poor diffusion barrier characteristics.[8] Stability in hydrogen is a particularly important property for the Si based photovoltaic applications, where H passivation is a key processing step in the solar cell fabrication. These factors and the limited availability of In have motivated researchers all over the world to explore new and relatively inexpensive TCO materials. It is also thought that the new materials can offer more technical advantages, especially in terms of processibility and post-deposition stability. [10] With the improvement in properties of TCOs, the solar cell industry is expected to benefit the most among all the applications. The performance of solar cells is directly related to the characteristics of the TCO layer, which serves as a window layer to let light through and as a contact layer to harvest the useful electrical current. Currently, solar cells are mostly used for strategic applications; however, its widespread domestic use is prohibited by the exorbitant price of the solar energy conversion units. To make the solar units affordable, the efficiency of the devices should be increased by 30%. [18] Currently, best values of efficiencies are about 25% for the CIGS and GaAs based devices and single crystal thin film Si photovoltaic cells. [19] These efficiencies have been achieved through careful device design and development of new materials technology. For example, for CIGS-based solar cells, the use of a sulfide or selenide-based transparent conductor would allow one to

employ only one type of deposition technique, [20] so it would be more economical and efficient to have a Se-based TC layer rather than a TCO.

New TCO materials should possess certain specific properties other than just high transparency and conductivity. With rapidly emerging applications, it becomes clear that work function, surface roughness, nano-structure, thermal and chemical reactivity or ease of patterning are critical TCO functionalities. Because the usefulness of TCO thin films depends on both their optical and electrical properties, both parameters should be considered together with environmental stability, abrasion resistance, electron work function, and compatibility with substrate and other components of a given device, as appropriate for a particular application. The availability of the raw materials and the economics of the deposition method are also significant factors in choosing the most appropriate TCO material. The selection decision is generally made by maximizing the functioning of a TCO thin film by considering all relevant parameters, and minimizing the expenses. TCO material selection based only on maximizing the conductivity and the transparency can be faulty.

Over the last 10 years, the field of transparent conducting oxides has dramatically increased with a huge influx in the number of active research groups and the diversity of materials and approaches. Recently, the scarcity and high price of indium needed for ITO, the most popular TCO, has spurred research aimed at finding a substitute. For an ideal TCO, electrical resistivity (ρ) should be ~10^{-4} Ω.cm or less, with an absorption coefficient (α) smaller than 10^4 cm^{-1} in the near-UV and VIS range, and with an optical band gap larger than 3eV. [21] A 100 nm thick film TCO film with these values for α and ρ will have optical transmission (T) 90% and a sheet resistance (R_S) 10 Ω. At present,

ZnO:Al (AZO) and ZnO:Ga (GZO) semiconductors are promising alternatives to ITO for thin-film transparent electrode applications. The best candidates is AZO, which can have a low resistivity, e.g. on the order of 10^{-4} Ω.cm, [22] and its source materials are inexpensive and non-toxic. However, the development of large area, high rate deposition techniques is needed for mass production.

Another objective of the recent effort to develop novel TCO materials is to deposit *p*-type TCO films. Most of the TCO materials are *n*-type semiconductors, but *p*-type TCO materials are required for the development of transparent electronics. Such *p*-type TCOs include: NiO, NiO:Li, $CuAlO_2$, Cu_2SrO_2, and $CuGaO_2$ thin films. These materials have not yet found a place in actual applications. Published reviews on TCOs reported exhaustively on the deposition and diagnostic techniques, on film characteristics, and expected applications. [20, 23]

1.2. BASIC PHYSICS OF TRANSPARENT CONDUCTIVE OXIDES

Efficient transparent conductor characteristics are achieved in representatively simple metal oxide semiconductors such as In_2O_3, SnO_2, ZnO, and CdO. These conventional TCO hosts are *n*-type materials when degenerately doped and they share similar chemical, structural and electronic properties. In addition to these well known ones, continuous efforts are being made to find more *p*-type TCOs [24, 25, 26]. This part will discuss some of the relevant basic concepts mainly pertinent to the conventional TCOs.

Not many materials exhibit this unusual combination of high transmittance and electrical conductivity. The origin of such an interesting display of properties can be best

understood by analyzing the band structures of these materials. Ordinarily, various materials can be classified into three categories based on their band structures as shown in Figure 1.1: (1) conducting metals (left), (2) semiconductors (middle) and (3) insulator (right). Based on the band structure analysis, a transparent material is an insulator which possesses completely filled valence and empty conduction bands; whereas metallic conductivity appears when the Fermi level lies within a band with a large density of states to provide high carrier concentration.

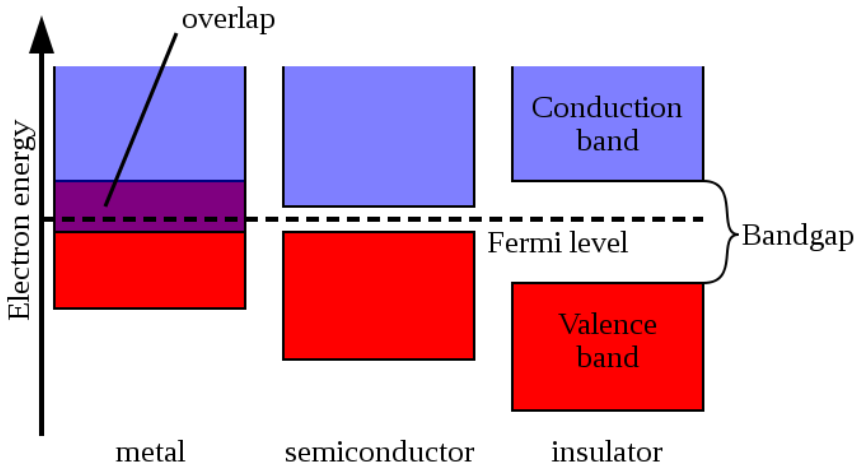

Figure 1.1 Materials categories based on their band structures

In oxides of main group metals, such as In_2O_3, SnO_2, and ZnO, strong interactions between the oxygen 2*p* and metal n*s* orbitals give rise to electronic band structures qualitatively similar for all these oxides: the bonding and nonbonding O *2p* states form the valence band while the conduction band arises from the anti-bonding M*s*-O*p* interactions. M*s*-O*p* interactions result in a gap between the valence and the conduction bands [27]. Therefore, in the undoped stoichiometric state, these materials

are insulators with optical band gap of about 3eV. To become a transparent conducting oxide (TCO), these TCO hosts must be degenerately doped to displace the Fermi level up into the conduction band. The partial density of states plots, reveal that the oxygen 2*p* and metal n*s* states make similar contributions to the conduction band. This provides a three-dimensional M*s*-O*p* network for charge transport once extra carriers fill the band.

The transparent conductors show relatively high values of electrical conductivity which does not preclude these TCO materials from exhibiting high transmittance. As Figure 1.2 shows, the high energy dispersion of the conduction band is the key feature of the TCO electronic structure. It ensures a pronounced Fermi energy displacement up above the conduction band minimum, the Burstein-Moss (BM) shift [28, 29]. The shift helps to broaden the optical transparency window and to keep the intense optical transitions from the valence band out of the visible range. The shift also gives rise to inter-band optical transitions from the valence band, E_v, and from the partially filled conduction band up into the next empty band, E_c, as well as to intra band transitions within the conduction band, E_i. [30-36] Owing to the high dispersion of the conduction band bottom, the density of states at the conduction band maximum is low and, hence, the optical absorption is low.

Thus, the unique properties possessed by TCOs have generally been explained by the combination of a large fundamental band gap and an inherent non-stoichiometry, or the ability to be doped in order to produce free electrons [35]. Materials with a wide band gap of 3eV or more behave as insulators at room temperature in the undoped state. After being doped to degeneracy by increasing the free carrier density enough to move the Fermi level up into the conduction band, these materials can become conductors. Here,

degenerate doping requires a source of electron donors in the form of point defects like oxygen vacancies or impurities with ionization energy close to the conduction band, which limits the materials exclusively to oxides of the post-transition metals with $(n-1)d^{10}ns^2$ electronic configurations [27], because of their relatively small band gaps as compared, for example, to light metal oxides Al_2O_3, CaO, or SiO_2.

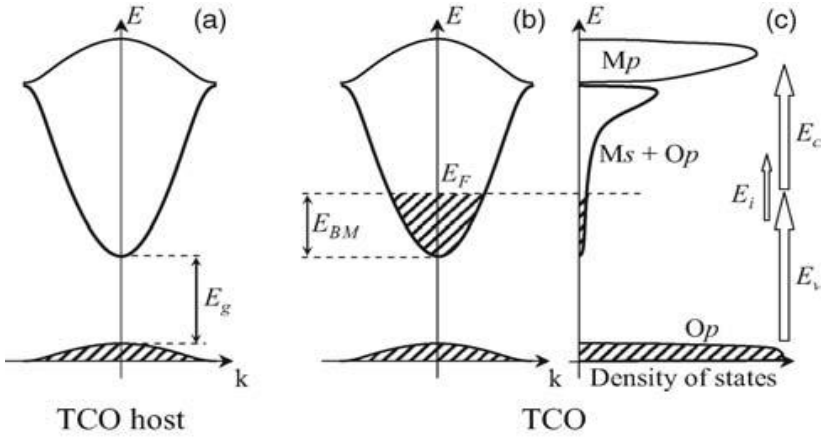

Figure 1.2 The Burstein-Moss (BM) shift in TCOs

Due to doping either by oxygen vacancies or by extrinsic dopants, the TCOs may possess conductivity σ within the range 10^2 – 10^6 (S/cm). [36] For most of the TCOs, which are n-type TCOs, the electrical conductivity depends on the electron density in the conduction band and on their mobility: $\sigma=\mu n e$, where μ is the electron mobility, n is its density, and *e* is the electron charge. The mobility is given by

$$\mu = \frac{e\tau}{m^*}$$

where τ is the mean time between collisions (the relaxation time), and m^* is the effective electron mass. However, as n and τ are negatively correlated, the magnitude of μ is

limited, making the conductivity σ to be intrinsically limited for two reasons. First, n and μ cannot be independently increased for practical TCOs with relatively high carrier concentrations. At high conducting electron densities, carrier transport is limited primarily by ionized impurity scattering, i.e., the Coulomb interactions between electrons and the dopants. [37] Higher doping concentration reduces carrier mobility to a degree that the conductivity is not increased; in addition, it decreases the optical transmission at the near-infrared edge. With increasing dopant concentration, the resistivity reaches a lower limit, and does not decrease beyond it, whereas the optical window becomes narrower. The resistivity of transparent conductive oxides (ITO, SnO_2, ZnO) are limited by ionized impurity scattering for carrier concentrations above $10^{20}cm^{-3}$ appears in Ref.[38]. In ITO films, the maximum carrier concentration was about $1.5\times10^{21}cm^{-3}$, and the same conductivity and mobility limits also held.[39] This phenomenon is a universal property of other semiconductors.[40] All recently developed TCO materials, including doped and undoped binary, ternary, and quaternary compounds, also suffer from the same limitations. [41] There is a large number of TCOs, but the high quality *p*-type TCOs are quite rare compared to *n*-type TCOs.[42] The monopolarity of existing TCOs results from the lack of intrinsic *p*-type wide band gap oxide semiconductors, and the difficulty in bipolar doping of wide band gap semiconductors [43]. Additionally, in most metal oxide semiconductors holes are strongly localized due to the strong Coulomb force exerted on holes by oxygen ions [44], which impedes hole conductivity. *P*-type doping in TCOs is difficult due to the lack of suitable dopants and low formation energy of native donors. As acceptors are introduced into the system, the Fermi Level shifts towards the valence band maximum and native donors are formed to compensate the change in Fermi

Level [43]. Some new p-type conducting TCOs have been found recently, [30, 45, 46, 47] which will benefit the semiconductor devices.

The second factor that limits the conductivity is that high dopant concentration could lead to clustering of the dopant ions. The scattering rate will be increased significantly and nonparabolicity of the conduction band will also be produced, which has to be taken into account for degenerately doped semiconductors with filled conduction bands. [48, 49]

The coexistence of high conductivity and high transparency arises from the formation of defect energy levels that can either donate electrons (*n*-type) to the conduction band or accept electrons (*p*-type) from the valence band. In wide band gap oxide conductors intrinsic defect levels form due to vacancies or interstitial atoms, where oxygen vacancies or interstitial metal ions result in donor states, and metal ion vacancies or oxygen interstitials result in acceptor states. [43] Most TCOs are intrinsically *n*-type because unbound metal ions form donor levels near the conduction band. *N*-type TCOs with high carrier concentrations have ever been shown to exhibit metal-like conductivity [44]. This research work focus on the electronic properties of TC both n and *p*-type hosts. Finding the most promising TC candidate can be viewed as a first step toward novel TC for various application and the criteria mentioned above.

1.3. PROPOSED RESEARCH AND OBJECTIVES

Conventional TCOs are considered as the foundation of the TCOs theory. Therefore, one of the research goals in this work is to investigate the conventional TCOs. In_2O_3, SnO_2, ZnO and CdO were explored in the first place. The related electronic and

optical properties provide a theoretical fundamental for this work. In this study, the calculated results include electronic band structure, density of states, electron effective mass and hole effective mass. All the calculations are completed by density function theory (DFT) within local density approximation (LDA) and the methods are presented in Section 2. The discussion about conventional TCOs is covered by Section 3. All the results obtained for the conventional TCOs were used as the control materials for every series of compounds that were investigated in this research. For instance, In_2O_3 is considered as the center of the first group materials that are discussed in Section 4; for ZnX (X=O, S, Se and Te) series, ZnO is treated as the standard for other ones.

Based on the understanding of the electronic structure characteristics in conventional TCOs, the second objective of this research work is to find the most promising transparent conductive candidates. As stated in the background section, the new TC candidates are a high demand due to the dramatic increase of the TC market. In this study, searching for potential TC candidates was carried out based on the comparative investigations of materials with similar electronic properties. Starting with the conventional TCOs, the main group metal oxides were considered as the first group of targets. Following the column and row chains of the periodic table, for instance, the related electronic properties of $Al_2O_3 \rightarrow Ga_2O_3 \rightarrow In_2O_3 \rightarrow Tl_2O_3$ and $Ag_2O \rightarrow CdO \rightarrow Ga_2O_3 \rightarrow In_2O_3 \rightarrow SnO_2$ were calculated. These two series are discussed in details in section 4.2 in Section 4. The searching work among the main group metal oxides covered all the elements in main groups. Besides the series compounds of In_2O_3 "targets", all the calculated results of the main group metal oxides are also presented in Section 4.5 in Section 4.

Furthermore, changing the anion element was also considered. Down through the column of oxygen, main group metal monochalcogenides, such as $In_2O_3 \rightarrow In_2S_3 \rightarrow In_2Se_3 \rightarrow In_2Te_3$, were investigated. In Section 4.2 two series of monochalcogenides, ZnX and CaX, are discussed in detail. Also, along the row of oxygen, interest has been drawn to nitrides and fluorides. Especially, GaN has already been reported as a new TC candidate [50]. Therefore, some nitrides and fluorides were considered and compared to GaN. The analysis regarding nitrides and fluorides is presented in Section 4.3 of Section 4. The last section gives the conclusions along with the future directions of this research work.

2. RESEARCH METHODOLOGY &APPROACH

2.1. DENSITY FUNCTION THEORY

The description of the physical properties of interacting many-particle systems has been one of the most important goals of physics during this century. The problem is to derive the properties of many-particle systems from the quantum mechanical laws of nature. This requires the solution of a partial differential equation (the Schrödinger or Dirac equation) of 3N spatial variables and N spin variables (for electrons) where N is the number of particles in the system. During the past decade, computer simulations based on a quantum-mechanical description of the interactions between electrons and atomic nuclei have had an increasingly important impact on materials science, [51] not only in fundamental understanding but also with a strong emphasis toward materials design for future technologies. The simulations are performed with atomistic detail by solving the Schrödinger equation to obtain energies and forces, and require only the atomic numbers of the constituents as input, and should describe the bonding between the atoms with high accuracy. The Schrödinger equation for the complex many-atom, many-electron system is not analytically solvable, and numerical approaches have become invaluable for physics, chemistry, and materials science.

Recent advances in computer calculation techniques and hardware technology have accelerated theoretical approaches to developing new materials. [52] Trial-and-error approaches are still needed to finely adjust the functions of developed materials to practical applications, but in some cases, the basic direction for materials development can be obtained from theoretical and computational considerations. A breakthrough in these computational efforts was realized in 1964 when Walter Kohn and coworkers

developed the density functional theory (DFT), a theory based on electron density, which is a function of only three spatial coordinates. [53] The Kohn–Sham equations of DFT cast the intractable complexity of the electron–electron interactions into an effective single-particle potential determined by the exchange-correlation functional. This functional (i.e., a function whose argument is another function) describes the complex kinetic and energetic interactions of an electron with other electrons. In the following part, the two core elements of DFT, which are Hohenberg-Kohn theorem and the Kohn-Sham equations, are presented.

2.1.1. Elements of DFT. The behavior of electrons in a crystal solid is governed by the many-body Schrodinger equation

$$\mathrm{H}\left|\Psi\right\rangle = \mathrm{E}\left|\Psi\right\rangle \tag{3.1}$$

It is generally appropriate to consider the electrons as either core or valence electrons. The core electrons are localized around the nuclei, and so the system can be treated as a number of valence electrons interacting with ion cores (nuclei and core electrons). Due to their significantly lower mass, the valence electrons can be assumed to react almost instantaneously to the motion of the ions - the ions appear stationary to the electrons, whereas the ions only respond to the time-averaged behavior of the electrons. This is the *Born-Oppenheimer* (or *adiabatic*) *approximation*, allowing the motion of the ions to be decoupled from that of the electrons. A stationary electronic state is then described by a wavefunction $\Psi(\vec{r}_i,...,\vec{r}_N)$ satisfying the many-electron time-independent Schrödinger equation

$$\hat{H}\Psi = [\hat{T}+\hat{V}+\hat{U}]\Psi = [\sum_{i}^{N} -\frac{\hbar^2}{2m}\nabla_i^2 + \sum_{i}^{N} V(\vec{r}_i) + \sum_{i<j}^{N} U(\vec{r}_i,\vec{r}_j)]\Psi = \mathrm{E}\Psi \tag{3.2}$$

where, for the *N*-electron system, $\hat{H}$ is the Hamiltonian, *E* is the total energy, $\hat{T}$ is the kinetic energy, $\hat{V}$ is the potential energy from the external field due to positively charged nuclei, and $\hat{U}$ is the electron-electron interaction energy. The operators $\hat{T}$ and $\hat{U}$ are called universal operators as they are the same for any *N*-electron system, while $\hat{V}$ is system dependent. This complicated many-particle equation is not separable into simpler single-particle equations because of the interaction term $\hat{U}$.

Here, at the heart of DFT, two Hohenberg-Kohn theorems provide a way to systematically map the many-body problem with $\hat{U}$, onto a single-body problem without $\hat{U}$. The first H-K theorem demonstrates that the ground state properties of a many-electron system are uniquely determined by an electron density that depends only on 3 spatial coordinates. It lays the groundwork for reducing the many-body problem of N electrons with 3N spatial coordinates to 3 spatial coordinates, through the use of functionals of the electron density. The second H-K theorem defines an energy function for the system and proves that the correct ground state electron density minimizes this energy functional. The derivation and formalism for the H-K theory is shown as follows. In DFT, the key variable is the particle density $n(\vec{r})$ which for a normalized Ψ is given by

$$n(\vec{r}) = N\iiint d^3r_2 d^3r_3 ... d^3r_N \Psi^*(\vec{r},\vec{r}_2,...,\vec{r}_N)\Psi(\vec{r},\vec{r}_2,...,\vec{r}_N) \qquad (3.3)$$

The relation of equation 3.3 can be reversed, i.e. for a given ground-state density $n_0(\vec{r})$ it is possible, in principle, to calculate the corresponding ground-state wavefunction Ψ_0. In other words, Ψ_0 is a unique functional of n_0, [54]

$$\Psi_0 = \Psi[n_0]$$

and consequently the ground-state expectation value of an observable $\hat{O}$ is also a functional of n_0

$$O[n_0] = \left\langle \Psi[n_0] \middle| \hat{O} \middle| \Psi[n_0] \right\rangle$$

In particular, the ground-state energy is a functional of n_0

$$E_0 = E[n_0] = \left\langle \Psi[n_0] \middle| \hat{T} + \hat{V} + \hat{U} \middle| \Psi[n_0] \right\rangle$$

where the contribution of the external potential $\left\langle \Psi[n_0] \middle| \hat{V} \middle| \Psi[n_0] \right\rangle$ can be written explicitly in terms of the ground-state density n_0

$$V[n_0] = \int V(\vec{r}) n_0(\vec{r}) d^3r$$

More generally, the contribution of the external potential $\left\langle \Psi \middle| \hat{V} \middle| \Psi \right\rangle$ can be written explicitly in terms of the density $n(\vec{r})$,

$$V[n\ ] = \int V(\vec{r}) n(\vec{r}) d^3r$$

The functionals $T[n]$ and $U[n]$ are called universal functionals, while *V[n]* is called a non-universal functional, as it depends on the system under study. Having specified a system, i.e., having specified V, one then has to minimize the functional

$$E[n] = T[n] + U[n] + \int V(\vec{r}) n(\vec{r}) d^3r$$

with respect to $n(\vec{r})$, assuming one has got reliable expressions for $T[n]$ and $U[n]$. A successful minimization of the energy functional will yield the ground-state density n_0 and thus all other ground-state observables.

The variational problems of minimizing the energy functional $E[n]$ can be solved by applying the Lagrangian method of undetermined multipliers.[55] First, one considers an energy functional that doesn't explicitly have an electron-electron interaction energy term,

$$E_s[n] = \left\langle \Psi_s[n] \middle| \hat{T} + \hat{V}_s \middle| \Psi_s[n] \right\rangle$$

where $\hat{T}$ denotes the kinetic energy operator and $\hat{V}_s$ is an external effective potential in which the particles are moving, so that $n_s(\vec{r}) \overset{def}{=} n(\vec{r})$.

Thus, one can solve the so-called Kohn-Sham equations of this auxiliary non-interacting system,

$$\left[-\frac{\hbar^2}{2m}\nabla^2 + V_s(\vec{r}) \right] \phi_i(\vec{r}) = \varepsilon_i \phi_i(\vec{r})$$

which yields the orbitals ϕ_i that reproduce the density $n(\vec{r})$ of the original many-body system

$$n(\vec{r}) \overset{def}{=} n_s(\vec{r}) = \sum_i^N \left| \phi_i(\vec{r}) \right|^2$$

The effective single-particle potential can be written in more detail as

$$V_s(\vec{r}) = V(\vec{r}) + \int \frac{e^2 n_s(\vec{r'})}{\left| \vec{r} - \vec{r'} \right|} d^3r' + V_{XC}\left[n_s(\vec{r}) \right]$$

where the second term denotes the so-called Hartree term describing the electron-electron Coulomb repulsion, while the last term V_{xc} is called the exchange-correlation potential. Here, V_{xc} includes correlation and exchange interactions. Since the Hartree term and V_{xc}

depend on $n(\vec{r})$, which depends on the ϕ_i, which in turn depend on V_s, the problem of solving the Kohn-Sham equation has to be done in a self-consistent (i.e., iterative) way. Usually one starts with an initial guess of $n(\vec{r})$, then calculates the corresponding V_s and solves the Kohn-Sham equations for the ϕ_i. From these, one calculates a new density and starts again. This procedure is then repeated until desired convergence is reached.

2.1.2. Making DFT Practical. The major problem with DFT is that the exact functional for exchange and correlation are not known. The functional is not known. The value of the functional for a uniform density $n(r) = n_0$ is known. However, approximations exist which permit the calculation of certain physical quantities quite accurately and make the DFT practical. In physics the most widely used approximation is the local-density approximation (LDA), [56] where the functional depends only on the density at the coordinate where the functional is evaluated:

$$E_{XC}^{LDA}[n] = \int \varepsilon_{XC}(n) n(\vec{r}) d^3 r$$

The LDA turned out to be computationally convenient and robust. In the LDA, the exchange-correlation energy is taken from the known results of the many-body electron interactions in an electron system of constant density. The LDA amounts to the following picture: at each point in a molecule or solid there exists a well defined electron density; it is assumed that an electron at such a point experiences the same many-body response by surrounding electrons as if the density of these surrounding electrons had the same value throughout the entire space as at the point of the reference electron. The exchange-correlation energy of the total molecule or solid is then the integral over the contributions from each volume element. It should be noted here that LDA is known to

underestimate the band gap value in semiconductors and insulators. Because the valence and conduction band dispersions are less affected by the LDA feature, often a so-called “scissors” operator is used to push the conduction band up so that the band gap corresponds to experimental value.

Thus, real systems, such as atoms, molecules, clusters and solids, are simultaneously inhomogeneous (the electrons are exposed to spatially varying electric field produced by the nuclei) and interacting (the electrons interact via the Coulomb interaction). The way density-functional theory in the local-density approximation, deals with this inhomogeneous many-body problem is by decomposing it into two simpler (but still highly nontrivial) problems: the solution of a spatially homogeneous interacting problem (the homogeneous electron liquid) yields the uniform exchange energy, and the solution of a spatially inhomogeneous noninteracting problem (the inhomogeneous electron gas described by the KS equations) yields the particle density. Both steps are connected by the local-density potential (57), which shows how the exchange energy of the uniform interacting system enters the equations for the inhomogeneous noninteracting system. The particular way in which the inhomogeneous many-body problem is decomposed, and the various possible improvements on the LDA are behind the success of DFT in practical applications of quantum mechanics to real materials.

2.1.3. Evolution of DFT Method. Prior to the developments of DFT, the calculation of energy band structures for crystalline solids had become the major goal of computational solid state physics. In computational solid states physics, total energy calculations as a predictive tool for crystal structures and elastic properties of solids came into general use only in the mid to late 1970’s. [58]

By 1970, DFT had become a widely accepted many-body approach for first principles calculations on solids. [58] Initially, energy band structure methods such as the augmented plane wave (APW) method and the KKR method were very tedious since the system of equations to be solved in each iterative step of self-consistency procedure were nonlinear. [59] Furthermore, the computer hardware at that time was limited in processor speed, but perhaps even more by memory size. A major step forward was the introduction of linearized methods, especially the linearized augmented plane wave (LAPW) and the linearized muffin-tin orbital (LMTO) method. [60] In this research work, the LMTO method is employed and the following part will introduce this method in some details. By 1980, computational solid state physicists worked on the formulation of all-electron self-consistent methods without muffin-tin shape approximations, such as the full-potential linearized augmented plane wave (FLAPW) method with total energy capabilities. [61] In the following decades, the methods based on DFT have been proved surprisingly successful in the academic field.

Thus, calculations based on density functional theory can be used to predict physical behavior of solids that originates from the nature of atomic bonding; and quantities such as electronic structure can be studied from a fundamental perspective. DFT opens a new door to innovative research on materials across physics, chemistry, materials science, surface science, and nanotechnology, and extending even to earth sciences and molecular biology. [62] This fascinating theory, which has been employed as a basic research methodology, provides a convincing and complete theoretical system for this investigation of TCOs.

2.2. OVERVIEW OF LMTO-ASA

LMTO is an acronym for Linear Muffin-Tin Orbital, which is a basis set for ab initio electronic structure calculations; it was originally formulated (together with the LAPW method --- Linear Augmented Plane Wave method) by O. K. Andersen. [63] For a long time, LMTO was implemented in the Atomic Spheres Approximation (ASA), an additional approximation that replaces the proper charge density and potentials by their spherical averages. [64]

To understand the LMTO-ASA from a real-space, fixed-basis point of view it should start by describing the choice of the LMTO-ASA basis function. Instead of obtaining the basis from solutions of an isolated atom, an isolated muffin-tin sphere is considered. The muffin-tin sphere has radius s, defined by a spherical potential for $r < s$ and a flat potential outside. It is assumed that the kinetic energy for one electron outside the muffin-tin sphere is approximately zero and the solution of the Schrodinger equation outside the muffin-tin sphere reduces to the solution of Laplace's equation. The solution inside the sphere should match the one outside to make the orbital continuous and differential at the Wigner-Seitz sphere s. But the set of muffin-tin orbital will not be the LMTO-ASA basis. It is only used as an envelope in order to force the LMTO-ASA basis set to be continuous and differentiable in all space. Based on this approximation, the problem can then be divided in two parts. The first involves finding the canonical structure constant and depends only on structure (position of the sites in the given system). The second is to find the solution of the Schrödinger equation inside a given Wigner-Seitz sphere. The second part can be obtained independently from the rest of the problem if the spherical potential within the sphere is known. These solutions depend

strongly on the type of atom located at the site. For our calculation work, the main input information is the basis site for the atomic positions. [65]

LMTO-ASA was introduced in 1984. It quickly gave rise to a new era regarding the quantitative description of a wide range of characteristics: structural, energetic, electronic, optical, and magnetic properties. [66] Although other approximations and programs have been carried out in the past decade, LMTO-ASA is still one of the most active in various fields, because of its suitability and efficiency. In the rest of this thesis, topics of interest related to TCOs will be presented. There include: the band gap of main group metal oxides, effective masses, charge neutrality level, and partial density of states. All results are based on calculations using the LMTO-ASA.

3. STUDY IN MAIN GROUP METAL OXIDES

3.1. INTRODUCTION

As previous sections presented, due to the increasing demand and development of transparent conducting film technologies, more versatile and environmentally friendly materials that would potentially replace the current well known TCOs, In_2O_3, SnO_2, CdO and ZnO, are highly needed. In this part of the thesis, the search for novel TC candidates among main group metal oxides is presented. The aim of this work is not only to find the most promising candidates for TC applications, also, to investigate general trends in the basic electronic and optical properties of various compounds (metal oxides, nitrides, sulfides, selenides and fluorides) according to their cation or anion placement in the periodic table.

In_2O_3, ZnO, SnO_2, and CdO are all main group metal oxides. They have remarkable electronic optical properties as outlined in Section 1 and are already widely used in the industrial field. Degenerately doped In_2O_3 is known to provide the optimal electrical and optical properties. Undoped stoichiometric In_2O_3 possesses small effective mass, wide band gap, and the charge neutrality level is above the conduction band minimum. [67] Our first step is to calculate and analyze the electronic and optical properties of the neighbor compounds of this special material. So in the following part, oxides of Al, Ga, In, Tl and Ag, Cd, In, Sn are studied, as Figure 3.1 shows. These chains of materials around indium oxide to see how the electronic configuration of cation affects the basic properties in these target materials will be analyzed.

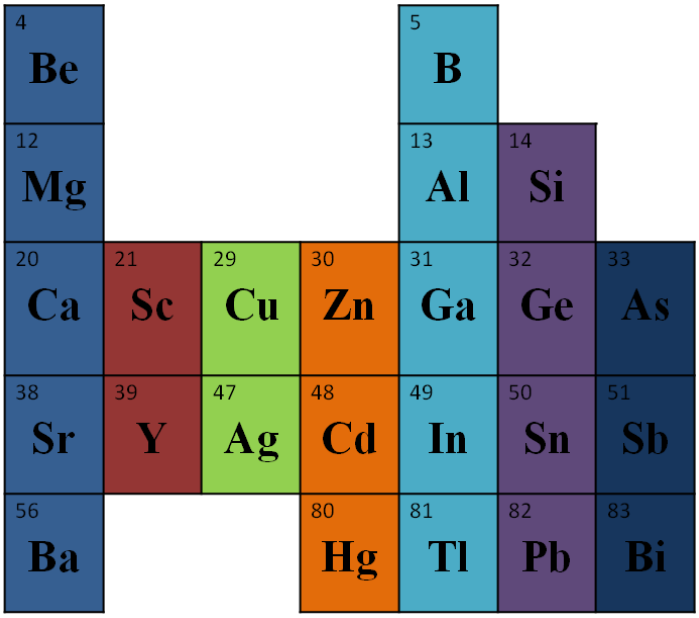

Figure 3.1 The metal elements calculated in the work showed in type of the periodic table

The first characteristic discussed in this part is the gap in the electronic band structure. Due to strong interaction between cations and anions, there is a well defined gap between the valence band and the conduction band. The band gap is expressed in terms of electron volts (eV), and the larger the band gap, the greater is the difficulty for the valence electrons to jump across the gap into the conduction band. This explains the poor electrical conductivity of wide-band gap insulators and semiconductors. Whenever there is an overlap of valence and conduction bands, electrons can move across freely into the conduction band as happens in the case of metals (conductors). If the band gap is narrow, electrons can be elevated to the conduction band with a small amount of energy. Such materials are semiconductors.

From the point of view of band gap, TCOs are classified as semiconductors with a wide optical band gap around 3eV. In this research, band gap is considered as one of the

criterion for finding potential TCO candidates. For In_2O_3, SnO_2, ZnO and CdO, their optical band gap, i.e. the direct gap, is about 3eV, which allows for optical transparency in the visible range (1.8eV-3.1eV). [68]

Following the investigation of the electronic band structure, the electron and hole effective masses are also analyzed. The electron movement in a lattice is different from the movement in free space. In a crystal, some electrons will pass through energy bands full of electrons and some with very few. By the definition of the effective mass m^*:

$$\frac{1}{m^*} = \frac{1}{\hbar^2} \cdot \frac{d^2\varepsilon}{dk^2} \ .$$

If the energy dispersion curves ε(k) (either from calculations or from measurements) is known, the effective masses can be determined and can also compare them to the free electron mass. The following interpretation (which can be fully justified theoretically) holds: If use the effective mass m^* of electrons and holes instead of their real mass m, it may be considered their behavior to be identical to that of electrons (or holes) in the free electron gas model. This applies in particular to their response to external forces. In this case, the deviation from the real mass takes care of the lattice part. Taken to the extremes, this may even imply zero or negative effective masses (e.g. exactly at or near the BZ boundary, where a force in the +x-direction may cause an electron to move in the –x direction because of the diffraction).

As the above expression, the sign of the effective mass depends on the curvature of the band. The decisive factor for the effective mass is thus the curvature of the dispersion line, as expressed in the second derivative. Large curvatures (= large second derivative = small radius of curvature) give small effective masses, small curvatures (=

small second derivative = large radius of curvature) give large ones. Small effective masses mean small (apparent) inertia or high mobilities μ. According to the formula for mobility, $\mu = e \cdot \tau_s / m^*$, the mobility goes up if effective mass is small.

In this work, the effective mass of the materials is obtained by fitting the calculated *E-k* diagram around the conduction band minimum (CBM) or the valence band maximum (VBM) by a parabola, which provides the electron and hole effective mass. In the Sections 3.3, 3.4 and 3.5, the results for the effective mass and band gaps will be presented. The results of calculations will be shown in regard to the current TCOs, and then the results in view of the search for potential TCOs will be discussed.

3.2. CRYSTAL STRUCTURE

A crystal structure of a solid is composed of a pattern, a set of atoms arranged in a particular way, and a lattice exhibiting long-range order and symmetry. Patterns are located upon the points of a lattice, which is an array of points repeating periodically in three dimensions. The points can be thought of as forming identical tiny boxes, called unit cells, that fill the space to create the lattice. The lengths of the edges of a unit cell and the angles between them are called the lattice parameters. The symmetry properties of the crystal are embodied in its space group. A crystal's structure and symmetry play a key role in determining many of its physical properties, such as electronic band structure, and optical transparency.

All begin with the basic information of the crystal structure. Table 3.1 lists the lattice space groups of the compounds along with the number of formula units in the unit cell (used in our band structure calculations) and the oxygen coordination of the cations.

Table 3.1. Structural and electronic properties of the Al-Tl and Ag-Sn groups of oxides. Crystal space group; the number of atoms per unit cell, N, used in the calculations; the coordination number (CN) of cation and anion; the obtained direct band gap E_g and experimental band gap E_{exp} in eV， the number of formula units per unit cell，Z.

Compound	Space #	N	Cation CN	Anion CN	E_g(eV)	E_{exp}(eV)	Z
Al_2O_3	167	10	6	4	6.45	9.2	2
α-Ga_2O_3	167	10	6	4	2.86	4.9	2
β-Ga_2O_3	12	10	6,4	4,3	2.29	4.61	2
In_2O_3	206	40	6	4	0.96	3.38	8
Tl_2O_3	206	40	6	4	-1	0.33	8
Compound	Space #	N	Cation CN	Anion CN	E_g	E_{exp} (eV)	Z
Ag_2O	224	6	4	2	0.23	1.4	2
CdO	225	2	6	6	-0.32	2.2	1
In_2O_3	206	40	6	4	0.96	3.38	8
SnO_2	60	36	6	3	1.76	3.41	12

Figure 3.2 shows the unit cells of the materials have been investigated. The two chains of compounds around the indium oxide, i.e. CdO, Ag_2O, and SnO_2, have three cubic and three hexagonal structures. In the figures of the crystal structures, the red color spheres represent the oxygen atoms and the other colors (green, blue) are the metal atoms. SnO_2 (space group 60) has the rutile structure, in which each tin atom is surrounded by six oxygens in an octahedral array, and each oxygen is surrounded by three tin atoms in a planar array. For In_2O_3 and Tl_2O_3, which both have the bixbyite structure, the oxygen form a close packed lattice and the metal ions lie at sixfold and fourfold interstices. The In sites are sixfold coordinated by oxygen. The overall symmetry is cubic, but the unit cell is large and has 40 atoms. The other oxide is CdO, which has

the rock-salt structure, with Cd or O ion surrounded by 6 neighbors. Ga_2O_3 has two phases with more complex crystal structures such as α-Ga_2O_3 and β-Ga_2O_3 structures. The β-Ga_2O_3, with a melting point of 1740˚C, [69] is the most stable crystalline modification.

Monoclinic (12)	Orthorhombic (60)	Rhombohedral (167)
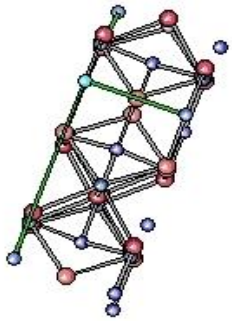	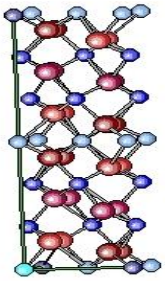	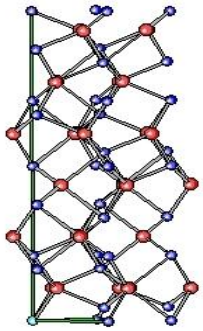
Cubic (206)	Cubic (224)	Cubic (225)
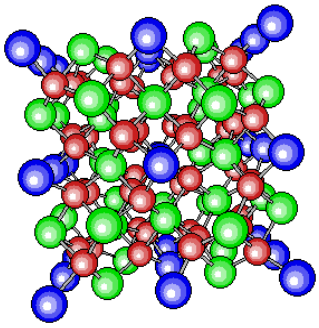	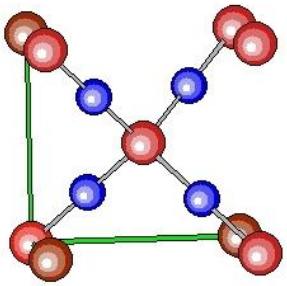	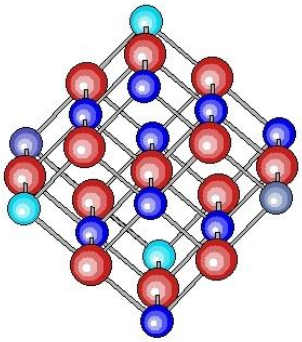

Figure 3.2 Crystal structures of Al-Tl and Ag-Sn groups of oxides: Metal atoms are shown in blue colors and the anion atoms are show in red colors. Oxygen is at the origin.

The oxide ions are in a distorted cubic close packing arrangement, and the gallium (III) ions are in distorted tetrahedral and octahedral sites. The Ga sites are both fourfold and sixfold coordinated. The Al_2O_3 has the same structure as α-Ga_2O_3. It has the corundum structure with $R\bar{3}c$ symmetry. The crystallographic cell consists of ten Ga_2O_3 or Al_2O_3 formula units. It has two independent lattice parameters *a* and *c*, and two internal coordinate variables *z*Metal and *x*O. The oxygen ions are approximately hexagonal close packed and the Ga/Al ions occupy two-thirds of the octahedral sites. Each Ga/Al octahedron shares one face and three edges with three other octahedra; the Ga/Al octahedra are moderately distorted in the lattice. Ag_2O is in a three-dimensional cuprite structure with covalent metal-oxygen bonding. It has the cubic structure and 2 formula units.

The crystal structure has a direct effect on the electronic properties of materials. In particular, the coordination of cations and anions and band length determine the overlap between the valence orbitals of neighboring atoms (metal and oxygen), which, in term, determines the band gap and effective mass. Thus, the structural peculiarities may result in specific features in the electronic band structure and also may suggest possible ways for efficient carrier generation. For example, empty space can serve as sites for interstitials, dopants, or guest atoms. Atoms from the structurally distinct layers or with unusual coordination may facilitate a defect formation, e.g., can be easily reduced to provide extra electrons which balance the charge neutrality, and lead to electrical conductivity.

3.3. ELECTRONIC BAND STRUCTURE

3.3.1. Comparison of Ag_2O, CdO, SnO_2 with In_2O_3. The discussion in this section will begin with the row of the compounds in which cations are neighbors of In in the periodic table. In this row, all compounds except Ag_2O, are well known and commonly used TCOs. Analysis of these compounds can lead to a clear understanding of the structural, electronic, and optical properties of TCOs and also can provide benefit for further work on prediction of TC candidates.

Electronic band structures calculated along the high symmetry directions in the corresponding Brillouin zones of the "neighbor oxides" of indium oxide are shown the Figure 3.3. All plots have the same energy scale so that the increase in the band gap value can be directly seen from the band structures. Table 3.1 lists the band gap values. As expected, the local density approximation (LDA) underestimates the band gap in all oxides. Our calculated band gap values are smaller by at least 2.45eV for In_2O_3 (for the direct band gap at Γ point), by 1.75eV for SnO_2, and by around 2eV for Ga_2O_3 and Al_2O_3 as compared to the available experimental optical data. [70, 71] For In_2O_3, CdO, and SnO_2, the obtained band gaps are similar to LDA results reported earlier [72]. One thing that needs to be noted is that the band gap underestimation does not affect the conclusions made.

First, from the band structure of In_2O_3, it can be seen that In_2O_3 has a single free-electron-like conduction band minimum. The value of the direct band gap at the Γ point between the CBM and VBM is 0.96eV. It has been noted that in some published papers, the band structure has been presented with the experimental band gap, which is achieved by a "scissors" operator, a rigid upward shift of the conduction band to obtain the

experimental value [73]. In this paper, all the plots of the band structure are the original plots from the LMTO-ASA calculation within LDA.

Based on the partial density of states in the conduction band for In_2O_3, Figure 3.4, the bottom of the conduction band is formed out of In 5*s* states. In a tight-binding description, it consists of 81% of In *s* states and the rest is from the contribution of In *p* (8%) and In *d* (11%) states. The upper valence band from -5.9eV up to 0eV consists mainly of O 2*p* states, mixed with small contributions of In *s* and *p* states. The upper valence band in In_2O_3 is typical of many oxides. It is relatively flat and thus has a large hole effective mass, which would significantly limit hole mobility, if hole doping is achieved. The results are consistent with the ultraviolet photoemission spectra of Christou et al. [74] and Klein [75]. Below the O 2*p* states, there are In 4*d* states, then O 2*s* states.

For SnO_2, a direct band gap of 1.76eV at the Γ point is found. Like In_2O_3, SnO_2 also has a free-electron-like conduction band with a single minimum. The valence band maximum has a Γ^{-2} symmetry, which leads to a direct forbidden band gap [76]. The upper valence band from 0eV down to -7.8eV consists mainly of O 2*p* states, mixed with some Sn *s* and *p* states. The upper valence band in SnO_2 is typical of many oxides. It is relatively flat, and thus has a large hole effective mass, which does not favor conduction by holes. The hole effective mass also will be discussed in detail in Section 3.5. The valence band is also consistent with the experimental ultraviolet photoemission spectra from R G Egdell's paper [77].

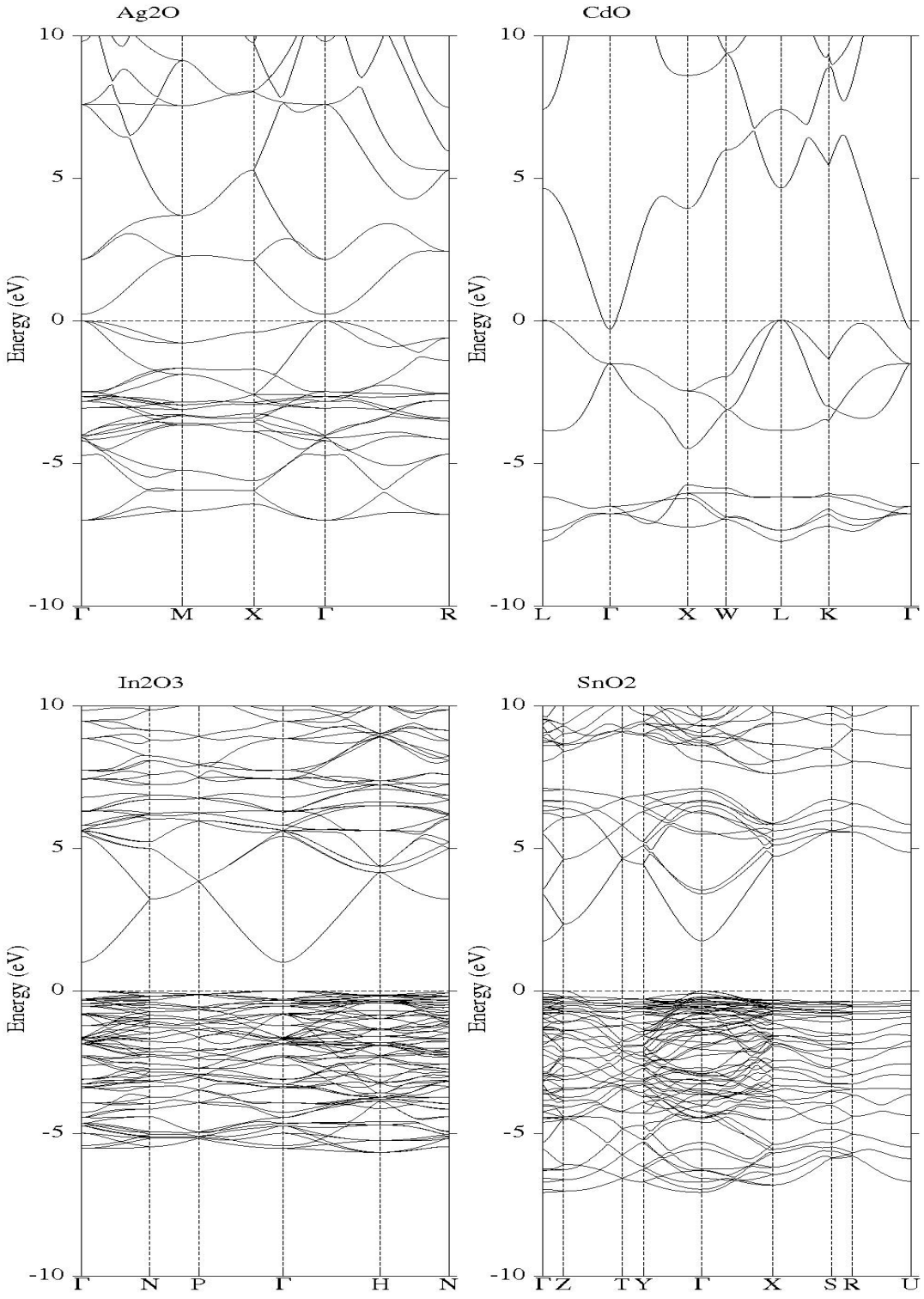

Figure 3.3 Electronic band structures of Ag_2O, CdO, In_2O_3 and SnO_2

CdO is also considered an n-type TCO like In_2O_3 and SnO_2. CdO has an indirect band gap, and because the LDA underestimates the band gap, the calculation finds that the gap becomes negative (VBM is higher than the CBM). From the band structure, it is clear to see that the conduction band minimum is at the Γ point and that the valence band maximum is not at the same point. The valence band maximum is displaced to the boundary L point. This is caused by the repulsion of the O *p* states in the upper valence band by Cd *d* states lying at -7.5eV. (Figure 3.3) The three upper valence bands in CdO consist mainly of O 2*p* states. However, instead of Cd *p* states leading to a downward repulsion of these states away from Γ, the upward repulsion of Cd *d* states is stronger.

Although Ag_2O is not one of the TCOs, it is an ideal candidate for a light absorption material in terms of energy conversion efficiency, and is appealing since it consists of non-toxic elements. From its band structure, the direct band gap at the Γ point has the value of 0.23eV is computed. As Table 3.1 shows, the computed band gap value increases in the set of compounds from Ag_2O to SnO_2: it is 0.23eV, -0.32eV, 0.96eV and 1.76eV, respectively. Sb_2O_3 was also calculated, with Sb being the element right after Sn in the same row in the periodic table. Sb_2O_3 has a computed direct band gap of 3.34eV. Thus, the band gap values follow the ordering $CdO < Ag_2O < In_2O_3 < SnO_2 < Sb_2O_3$. Although the order of CdO and Ag_2O is not what had been expected, the rest still follow the trend that $CdO < In_2O_3 < SnO_2 < Sb_2O_3$, which means that the band gap increases as the cation's period increases. Besides the electronic band structure, the partial density of states in the conduction band for these compounds is also calculated. In Figure 3.4, plots for Ag_2O, CdO, In_2O_3 and SnO_2 are shown. The blue lines are the metal *p* states and the red lines are the combination of the metal *s* states and oxygen *p* states. The partial

density of states provides a more rigorous identification of the nature of the conduction states in terms of participating orbitals.

From the In_2O_3 partial density of states plot Figure 3.4, it can been seen that strong interactions between the oxygen 2*p* and metal n*s* orbitals give rise to electronic band structures qualitatively similar for all these oxides: the conduction band arises from the antibonding M*s*–O*p* interactions. The empty *p* states of the metal ion form the next of band at a higher energy. This provides a three-dimensional M*s*–O*p* network for charge transport once extra carriers fill the band. In the group of partial DOS plots, the metal *p* states shift to a higher energy with respect to the conduction band minimum as the cation's period increases. Therefore for CdO, In_2O_3, and SnO_2, the metal *p* states are above the metal *s* and oxygen *p* network states. As a result, charge transport in properly doped systems will occur via the M*s*–O*p* network, even for a large carrier concentration, i.e. when the BM shift is large.

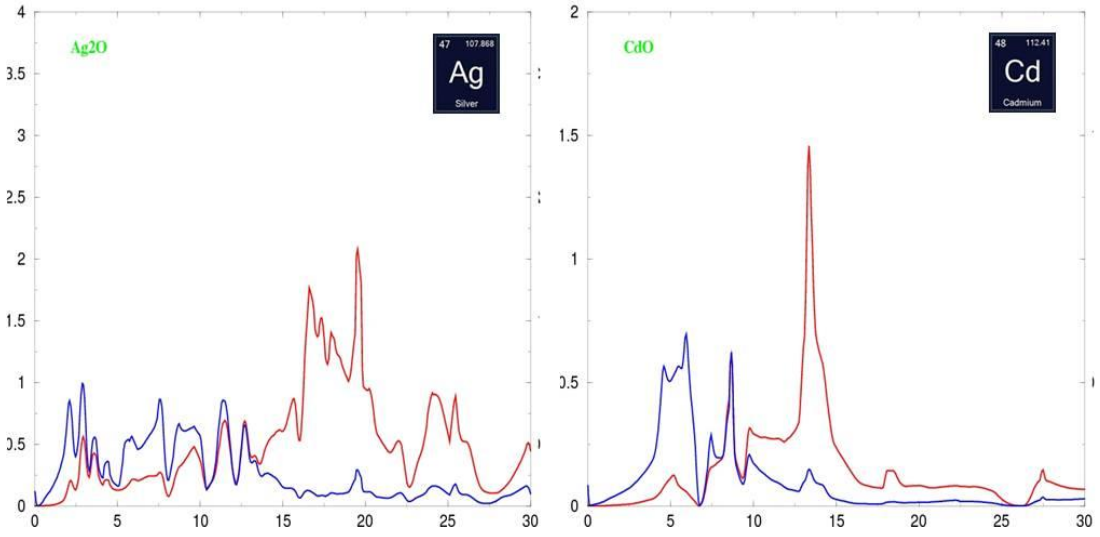

Figure 3.4 Partial density of states for Ag_2O, CdO, In_2O_3 and SnO_2: red lines are the metal *p* states and the blue lines are the combination of metal *s* states and oxygen *p* states.

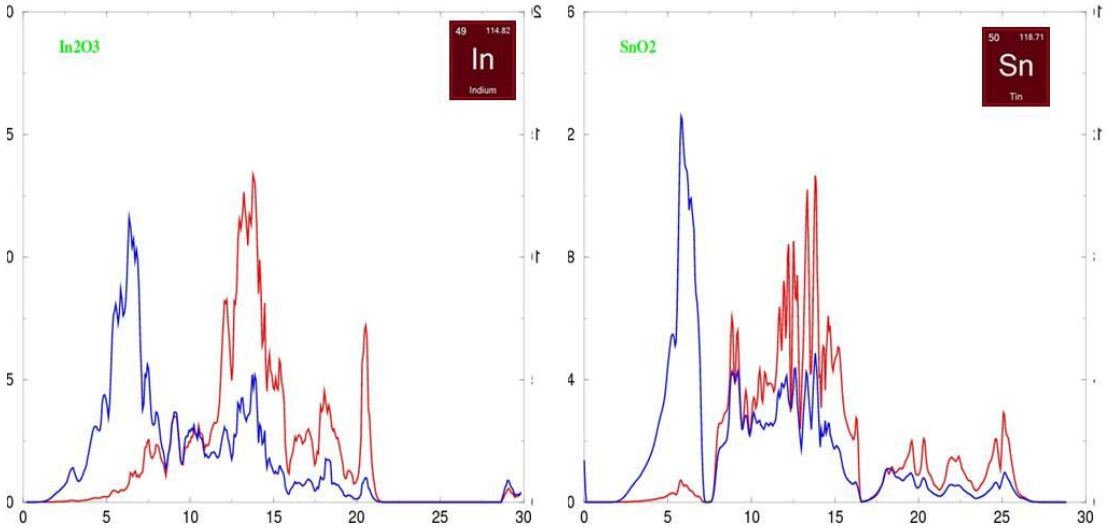

Figure 3.4 Partial density of states for Ag_2O, CdO, In_2O_3 and SnO_2: red lines are the metal *p* states and the blue lines are the combination of metal *s* states and oxygen *p* states. (cont.)

The spherical symmetry of the metal s orbitals and their strong hybridization with the *p* orbitals of the oxygen neighbors provides the most uniform charge distribution throughout the cell, which can lead to good carrier mobility. From the partial density of states shown in Figure 3.4, it is clear that Ag-p states are at a lower energy. Comparing the partial density of states of Ag_2O to CdO, it is noticeable that the bottom of the conduction band of CdO is mainly from the network of Cd *s* sates and O *p* states, which is the blue line in Figure 3.4. However, for Ag_2O, the contributions from the network Ag *s* states and O *p* states, and from the Ag *p* states are comparable near the conduction band.

The origin of the electron localization in oxygen reduced main group metal oxides was also investigated, showed in Table 3.2, and it correlates with the proximity of the cations *p*-states to the CB. The results are listed in the table. Usually, the metal *d* states will not contribute as much as it has been found in this work; actually, this is also caused

by the failure of LDA. Because the calculation based on the LDA underestimate the band gap, [78] the *d* states are closer to the conduction band minimum, and give a large contribution. The charge localized on defect neighboring atoms is increased from 10% to 40% as it goes from Ag_2O to SnO_2, which means that the percentage increases with the cation's period. For Ag_2O the charge localized on the defect neighboring atoms is only 10% and the contribution from cations is mainly from the *s* and *d* states, which have almost the same contribution. Compared to Ag_2O, the conventional TCOs, In_2O_3, and SnO_2 have larger charge localized near the defect, and most of the contribution is from the cations *s* states, which are 81% and 78%.

Table 3.2 Electron localization in oxygen deficient Ag_2O, CdO, In_2O_3, SnO_2

Oxide	**CL(%)**	**Contribution for cations nearest to defect (%)**		
		s	p	d
Ag_2O	10	52	5	43
CdO	18	79	3	18
In_2O_3	31	81	8	11
SnO_2	40	78	13	9

3.3.2. Comparison of Al_2O_3, Ga_2O_3, Tl_2O_3 with In_2O_3. In Figure 3.5, the band structures of Al_2O_3, Ga_2O_3, In_2O_3, and Tl_2O_3 are shown. This set of materials represents a column with all the cations belonging to the same group (IIIA) in the periodic table. From Table 3.1, it can be seen that the band gap value is decreasing as it moves from aluminum oxide to thallium oxide in the order $Al_2O_3 > Ga_2O_3 > In_2O_3 > Tl_2O_3$. This can also be seen from the band structure Figure 3.5. Unlike the row compounds it is considered that in the previous section, this group of materials is from light metal oxides to heavy metal oxides.

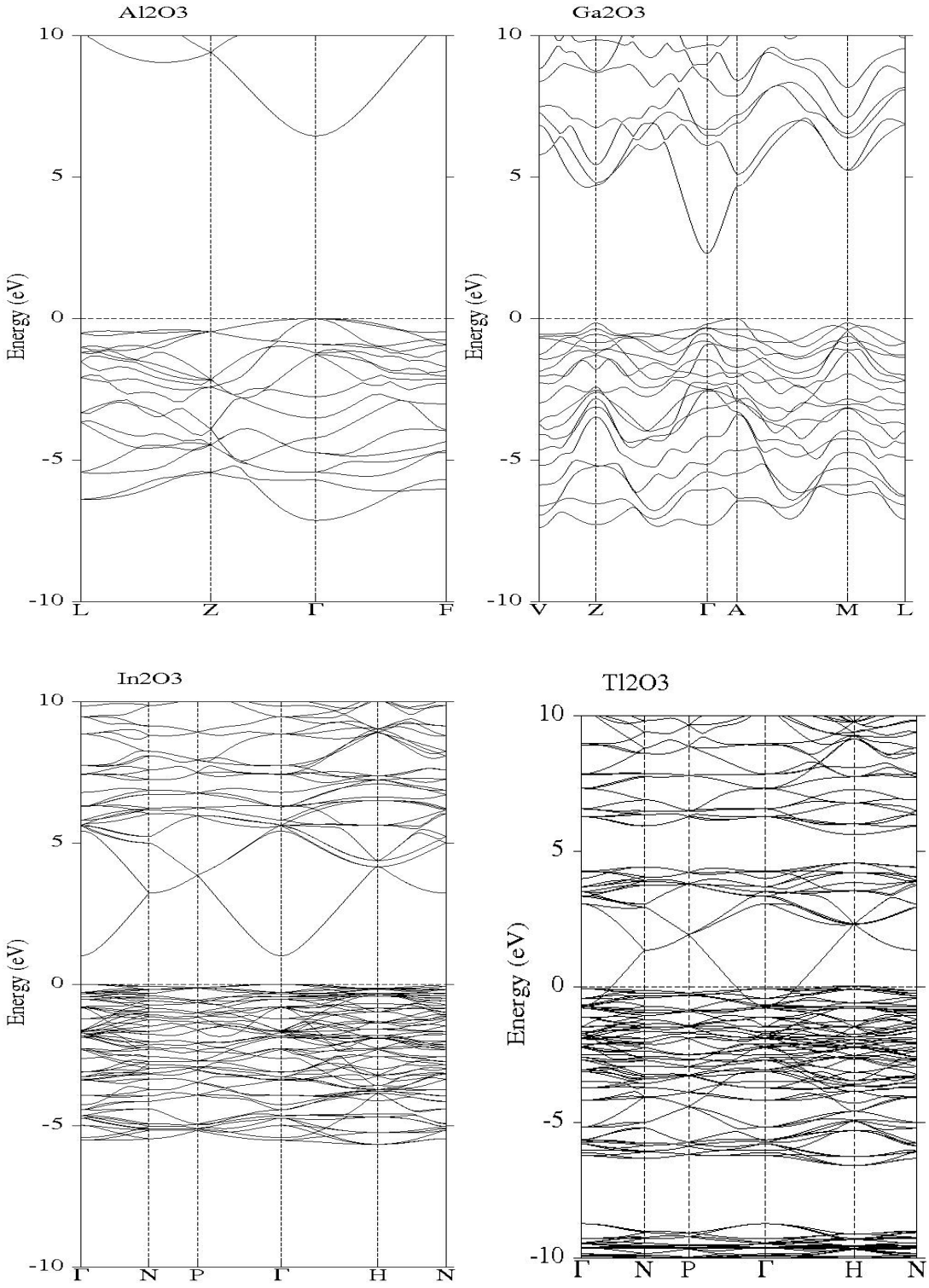

Figure 3.5 Band structures of Al_2O_3, Ga_2O_3, In_2O_3 and Tl_2O_3

In this section, the electronic band structure, partial density of states and the origin of electron localization will be also discussed.

Compared to In_2O_3, Al_2O_3 has a much larger band gap. Aluminum oxide is an electrical insulator but has a relatively high thermal conductivity for a ceramic material. In the present work, α-Al_2O_3 was calculated, which has a direct band gap of 6.45eV at the symmetry point Γ. The top of the upper valence bands of Al_2O_3 arises from O 2*p* nonbonding orbitals. These bands are flat in k space and correspond to states which are localized in real space forming the familiar O^{2-} ion. The bottom of the conduction band states arises from delocalized Al 3*s* and O 2*p* antibonding states. For β-Ga_2O_3, an indirect band gap of 2.29eV, with the valence band maximum (VBM) located slightly away from the Γ symmetry point has been obtained. The energy dispersion curves in the conduction band are shown along each of the reciprocal axis (approximately the direction of each axis in real space is parallel to that of corresponding axis in reciprocal space).

It is noticeable that the conduction band has a large dispersion around the Γ point, whereas the valence band is almost flat, indicating a very large hole mass. The effective mass will be discussed in the following section. Our band structure of Tl_2O_3 shows metallic properties, however, a similar situation to CdO where a negative band gap is obtained within the LDA is possible. Previous publications show that, despite its extremely high *n*-type conductivity, the electronic structure of Tl_2O_3 is still a cause for much debate. [79,80] It has been postulated for decades that Tl_2O_3 is a metallic conductor, [81–83] but conversely the carrier concentration is found to vary strongly with oxygen partial pressure, [84–86] which is indicative of a intrinsic defect induced, hence, Tl_2O_3 is of semiconducting nature.

The arguments that Tl_2O_3 is a semiconductor have been supported by the fact that many studies have reported it to possess optical band gaps varying from 1.40eV to 2.75eV. [81, 83, 86] Geserich reported the direct bang gap of Tl_2O_3 to be 2.20eV, with an indirect band gap of 1.40eV. [84]From the calculation, it is found that the conduction band minimum is at the Γ symmetry point, which is overlapped with the top of the valence band and the valence band maximum is also at the Γ point. As it was mentioned before, the LDA method underestimates the band gap, as it has proved for In_2O_3, SnO_2, and other compounds. So non-local approaches such as the screened exchange LDA method to investigate the fundamental band gap of Tl_2O_3 is therefore warranted.

Thus, for the group of oxides of metals from Al to Tl, it can be concluded that the band gap decreases. On the other hand, similar to discussion for In_2O_3, researchers can understand more from the partial density of states in the conduction band. It is widely accepted that the conduction band(s) in oxides of the main group metals is formed from the cations states. However, the detailed analysis of the partial DOS at the bottom of the conduction band (Figure 3.6) provides a different result: it has been found that the oxygen antibonding *p* states give similar contributions to those from the cations *s* states. This suggests that both the cation *s* and anion *p* states will be available for the transport of extra carriers, which will determine the electron mobility in these materials once they are degenerately doped.

Also, by plotting these four partial DOS within the same energy scale, it can be seen that, there is a formal trend from the Al to Tl. In Figure 3.6, the red color lines are metal *p* states and the blue lines are metal *s* states combined with the oxygen *p* states. The partial DOS provides the proximity of the cations *p*-states to the CB: the *p* states

move further from the conduction band as the cation's atomic number increases in the group.

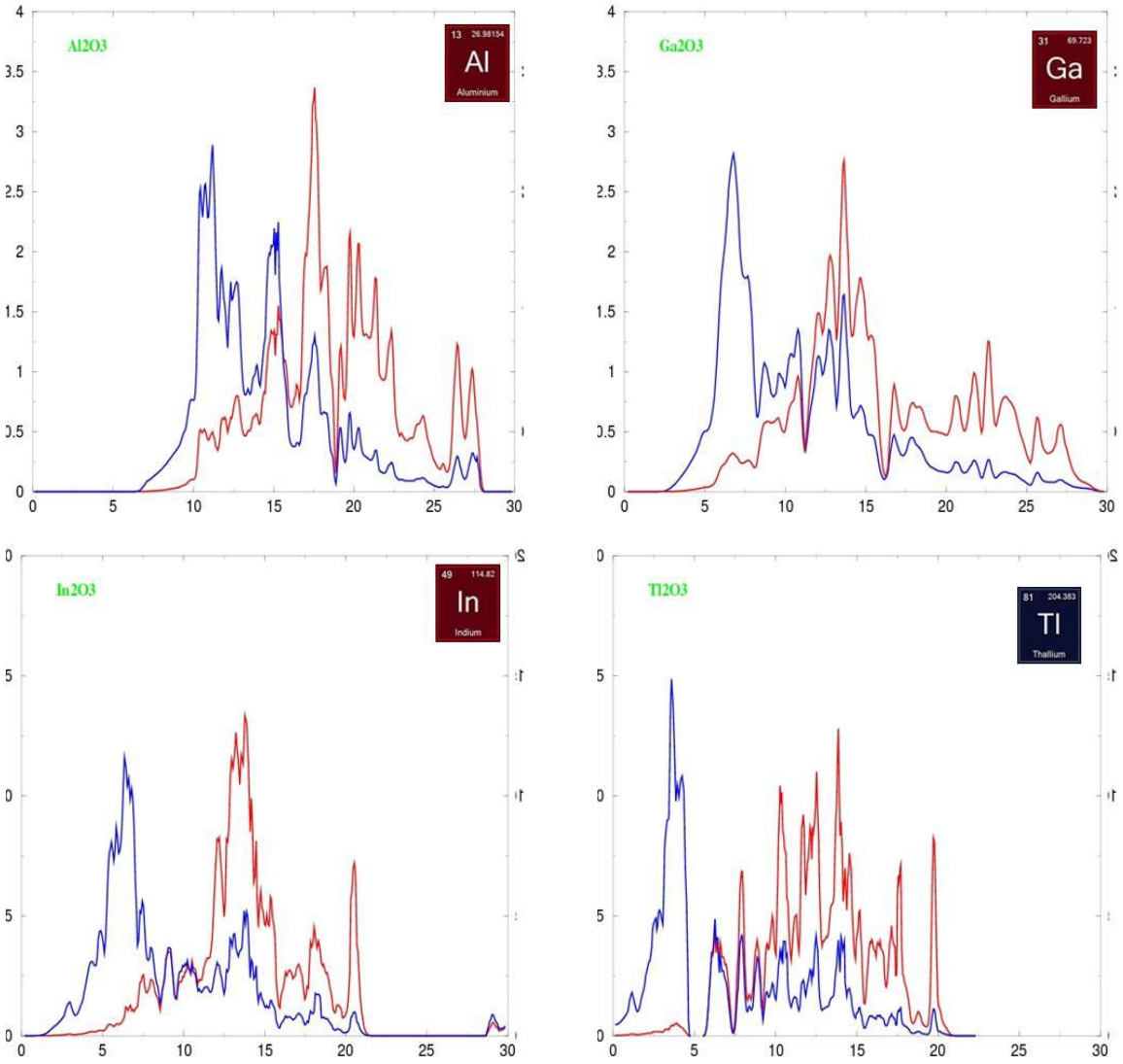

Figure 3.6 Partial density of states for Al_2O_3, Ga_2O_3, In_2O_3 and Tl_2O_3

Also, from the Table 3.3, it can be seen that the change of the charge localized on the oxygen defect neighboring atoms, which decreases by the same order of the cations. In this group of compounds, beside the cation period, there are more interested in the

comparison between the light metal oxides (Al_2O_3, Ga_2O_3) and the heavy metal oxides (In_2O_3, Tl_2O_3). The contribution for cations nearest to defect has been calculated, and it is noticeable that the metal *s* states contribution increases and that of the metal *p* states decreases from the Al to In.

Table 3.3 Electron localization in oxygen deficient Al_2O_3, Ga_2O_3, In_2O_3 and Tl_2O_3

Oxide	**CL(%)**	**Contribution for cations nearest to defect (%)**		
		s	p	d
Al_2O_3	87	30	47	23
Ga_2O_3	61	56	33	11
In_2O_3	31	81	8	11
Tl_2O_3	3	70	13	17

A comparison of the electronic band structure of stoichiometric undoped Al_2O_3 (Figure 3.5) with the one in the conventional In_2O_3 (Figure 3.5), reveals that the fundamental differences in the electronic properties of these oxides originate from the different energy location of the metal's empty *p* or *d* states with respect to the conduction band bottom. In In_2O_3, the metal *p* band is well above its s band (Figure 3.5). As it was mentioned before, this can provide good carrier transport.

Compared to In_2O_3, in Al_2O_3 *p* or *d* bands almost coincide with its *s* band (Figure 3.5). When an oxygen vacancy is created, the Al *p* orbitals are energetically available for the induced electrons. Strong binding of the highly anisotropic orbitals with the states of the nearest oxygen atoms lowers the total energy of the system. Naturally, the transition between In_2O_3 and Al_2O_3 is not abrupt. The proximity of the metal *p* or *d* states to the s-type conduction band bottom in oxide of a main group metal (with ns^2 electronic

configuration) will determine the orbital composition of the conduction band wavefunction. This point can be proved by the calculation for Ga_2O_3, the plot of partial DOS for α-Ga_2O_3 is showed in Figure 3.7. In oxygen-deficient β-Ga_2O_3, about 61% of the total cation contributions to the conduction band wavefunction comes from the Ga atoms nearest to the oxygen defect – to be compared with the same result for In_2O_3 (31%) on one side and Al_2O_3 (87%) on the other. In Ga_2O_3, the Ga p band is located relatively close to the metal s band but does not coincide with it exactly as, for example, in Al_2O_3 (Figure 3.5).

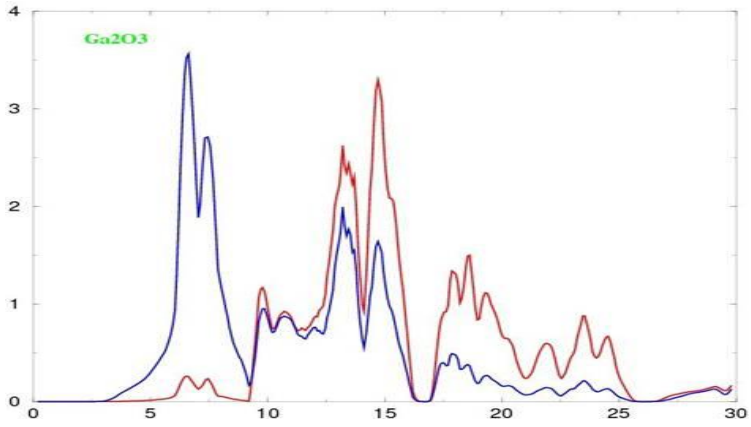

Figure 3.7 The partial density of states of α-Ga_2O_3

This leads to considerable but not dominant contributions from the Ga *p* states near the bottom of the conduction band. Hence, in Ga_2O_3, alternative carrier generation may give satisfactory results. In this work, α-Ga_2O_3 was also calculated, which is a higher symmetry phase than β-Ga_2O_3. In α- Ga_2O_3 the charge localized near the defect is 53%

and the *s* contribution is 66%. Compared to the charge localization of β-Ga_2O_3, which is 61%, it can confer that for higher symmetry phases, the detrimental *p*-states are located at higher energy.

3.4. ELECTRON EFFECTIVE MASS

As it was stated in the introduction section, the effective mass is proportional to the dispersion curvature in the electronic band structure. In this work the effective mass of electrons in the conduction band was calculated by fitting the dispersion of the calculated conduction band to a parabola: it has been obtained three values for each compound from the three directions, which are [1 0 0], [0 1 0] and [0 0 1] near the Γ point, i.e. the standard crystallographic directions, making it easier to compare to the experimental values.

In the Table 3.4, the electron effective masses for the neighbor oxides of In_2O_3 are presented. Compared to the band gaps, which is listed before (Table 3.1), the increase in both band gap and electron effective mass is consistent. The electron effective mass also decreases down the column or along the row. It needs to be point out here that the reason the electron effective mass is directly related to the band gap value, can be illustrated based on the **k*p** theory: the smaller the band gap, the smaller the electron effective mass, and vice versa. One more thing that can be noted from the Table 3.1 and Table 3.4, is that the band gap is 2.86eV for α-Ga_2O_3 and 2.29eV for β-Ga_2O_3; however, the effective mass is 0.2808m_e for α-Ga_2O_3 and 0.3206 m_e for β-Ga_2O_3, this can be explained by another factor which electron effective mass related to.

Table 3.4 Electron effective mass of the Al-Tl and Ag-Sn groups of oxides

Compound	$m_e^{[100]}$	$m_e^{[010]}$	$m_e^{[001]}$	Com	$m_e^{[100]}$	$m_e^{[010]}$	$m_e^{[001]}$
Al_2O_3	0.4067	0.4067	0.4175	Ag_2O	0.6634	0.6634	0.6634
α-Ga_2O_3	0.2808	0.2808	0.2215	CdO	0.2162	0.2162	0.2162
β-Ga_2O_3	0.3206	0.3206	0.2431	In_2O_3	0.1796	0.1796	0.1796
In_2O_3	0.1796	0.1796	0.1796	SnO_2	0.2646	0.2439	0.2196

The electron effective mass does not only depend on the band gap alone, and the overlap between the wave function of the neighboring atoms, i.e., between the cation s orbitals and the antibonding *p* orbitals of the oxygen atoms, also plays an important role. Therefore, in addition to the oxygen coordination, the distortions in the polyhedra and in the cation-anion chains affect the orbital overlap and hence affect the electron effective mass. Another way to explain that the electron effective mass of α- Ga_2O_3 is less than β-Ga_2O_3 despite the opposite trend in the band gap, is that α-Ga_2O_3 has a more symmetrical crystal structure than β-Ga_2O_3, which provides a larger orbital overlap.

From the band structure of CdO, it has an indirect band gap with the conduction band minimum at Γ and the valence band maximum at the L point. The electron effective masses given in Table 3.5 are calculated at the Γ point in three crystallographic directions as it was mentioned before. As proven in previous related work, [87] for the direction in the standard Brillouin zone, [1 1 1] or [0 1 1], the electron effective masses are the same. Thus, the effective mass is isotropic at the Γ point since the conduction band is parabolic near the wave vector **k**=0. This will be mentioned again in the following section, which will present the calculations for other oxides with an indirect band gap.

For the conventional TCOs, which have high energy dispersion at the bottom of the conduction band (Figure 3.3, Figure 3.5), the electron effective mass is small:

$0.1796m_e$, $0.2162m_e$ and $0.2646\ m_e$ for In_2O_3, SnO_2, and CdO, respectively, in our LDA calculation. The small electron effective mass should lead to a high carrier mobility upon degenerate doping of the materials. The electron effective masses found for Al_2O_3, α-Ga_2O_3, and β-Ga_2O_3 compounds are comparable to those in well-known and commercially utilized TCOs. The electron effective mass plays an important role to predict potential TC candidates; however it is not a necessary condition.

3.5. HOLE EFFECTIVE MASS

In Table 3.5, the hole effective masses are listed. The calculations for the hole effective mass follows the same process as the electron effective mass calculation, only now the valence band maximum are used hare. The hole effective mass can be understood as another interesting peculiarity of the electronic band structure plots, which is the large anisotropy of the top of the valence band. By detecting the value of the hole effective mass, the mobility of the carriers in the valence band can analyzed, which will benefit the search for potential *p*-type TC candidates, similar as it is considered, the electron effective mass for *n*-type TCOs. Although, it cannot assert the carrier mobility only based on the results of the hole effective mass, it can still be uses as one of our test standards for analyzing and discussion.

Table 3.5 Hole effective mass of the Al-Tl and Ag-Sn groups of oxides

Com	$m_h^{[100]}$	$m_h^{[010]}$	$m_h^{[001]}$	Com	$m_h^{[100]}$	$m_h^{[010]}$	$m_h^{[001]}$
Al_2O_3	2.4542	2.4542	0.9419	Ag_2O	2.7960	2.7960	2.7960
α-Ga_2O_3	3.3233	3.3233	1.5801	CdO	15.7308	15.7308	15.7308
β-Ga_2O_3	3.3233	3.3233	1.5801	In_2O_3	0.7868	0.7868	0.7868
In_2O_3	0.7868	0.7868	0.7868	SnO_2	1.9403	1.2783	16.8484

3.6. PREDICTIVE CALCULATIONS FOR MAIN GROUP METAL OXIDES

In this section, the work on searching for potential TC candidates within main group metal oxides will be presented. Figure 3.1 shows a part of the periodic table, which lists all the metal elements include in this work. As it has been known, there are countless metal oxides even only for the considered part of the periodic table. For the same metal oxides, at different temperature and pressure, they also can display different phases, which mean they have various structural, electronic and optical properties. So far 50 oxides have been calculated.

For this work, all the basic information for the compounds is from "The handbook of crystal structure" and the website of American Mineralogist Crystal Structure (http://rruff.geo.arizona.edu/AMS/). The data at 300k were chosen and also avoided the high pressure phases. Also, it has tried to find the crystal data from the latest reports, which would provide most accurate measurements. The main goal is to make our computational results convincing for further practical usage, especially, for further experimental testing work.

So far, the calculation for the crystal structure modeling, band structure, density of states, electron effective mass and hole effective mass are all completed for the materials listed in the Table 3.1. In this part of the thesis, this thesis will only summarize the results of the calculated band gap, electron effective mass and hole effective mass. As it was mentioned in the introduction to this section, the value of band gap (>3eV) and electron effective mass (~$0.2m_e$) are two main stunning properties of conventional TCO hosts. Although it cannot be fully concluded or predicted which compound is the most promising TC candidate, the process can work like a filter pick up the ones that satisfy

the two standards for further, more accurate calculation, or for experimental work. Meanwhile, by analyzing and comparing all the results, it will help us to understand the electronic and optical properties related to the chemical and structural characteristics.

3.6.1. Band Gap of Main Group Metal Oxides. The band gap of main group metal oxides is presented in the following charts. The results for the metal oxides were organized from the same column in the same group and the color for each data series match with the color in the periodic table (Figure 3.1). The calculated results for the band gap of main group metal oxides are shown in Figure 3.8.

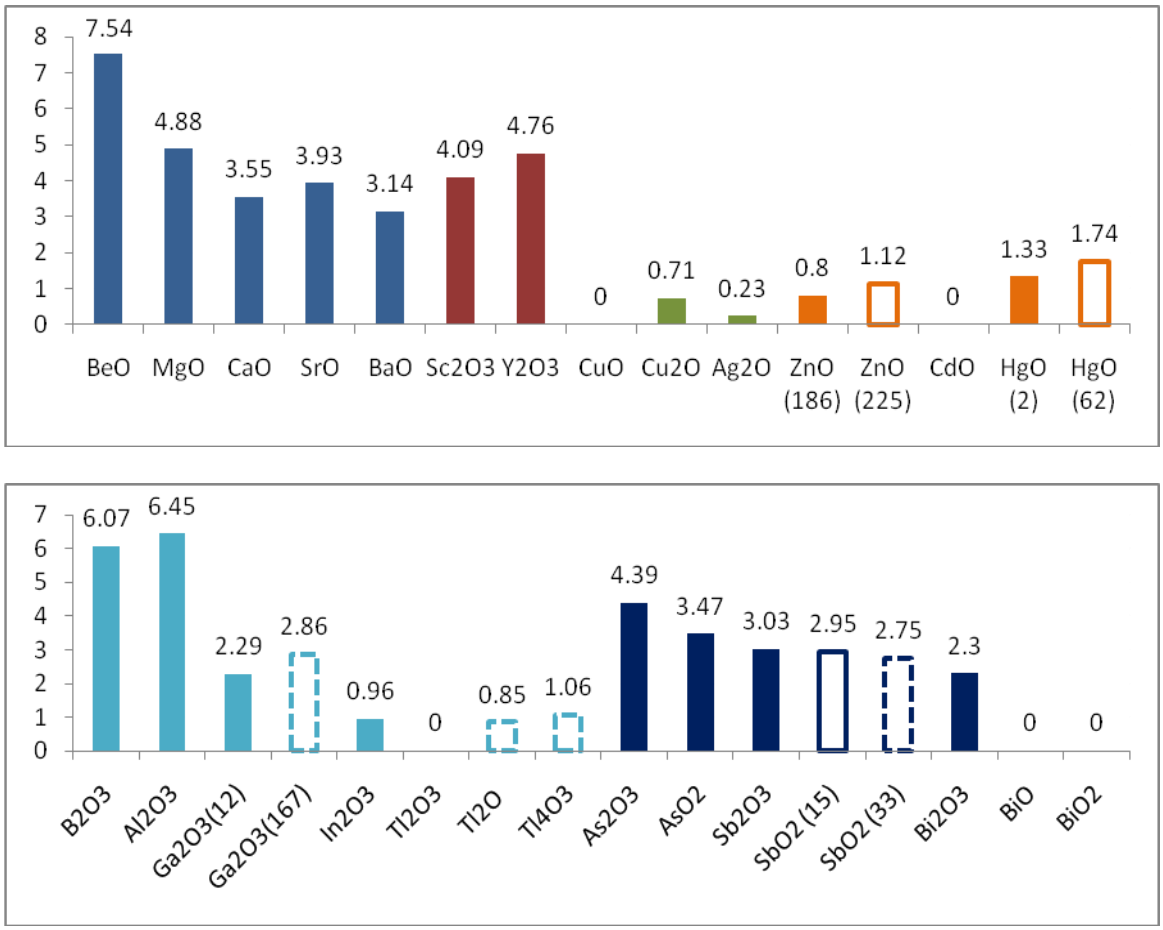

Figure 3.8 Band gap of main group metal oxides

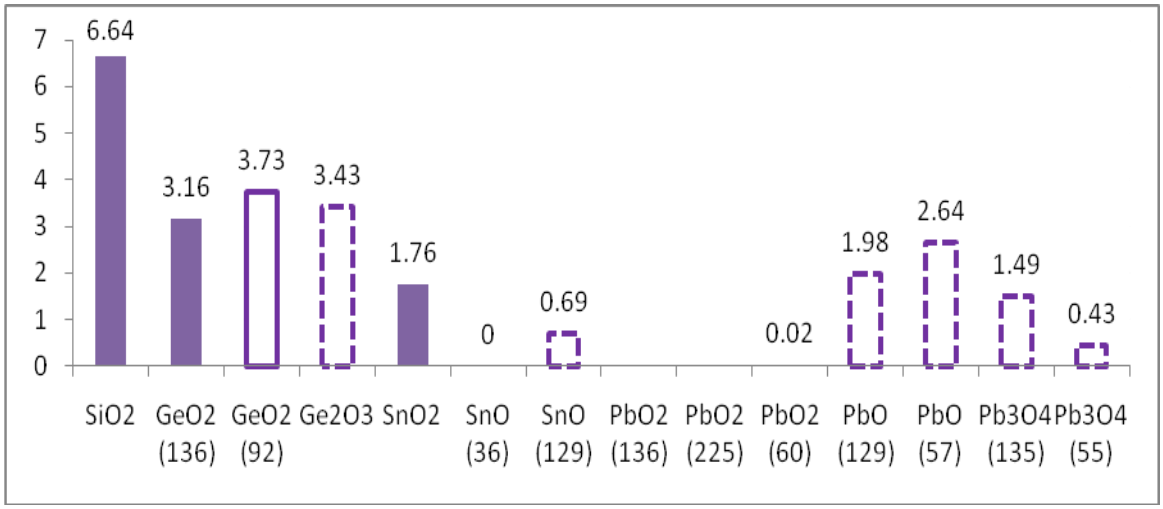

Figure 3.8 Band gap of main group metal oxides (cont.)

For some oxides, different phases and different oxidation states have calculated, e.g., for Sb oxides, there calculation for Sb_2O_3 and two phases of SbO_2, the space groups are 15 and 33. For each column, the band gap starts with the large band gap value. For instance, the first column begins with BeO, where the band gap is 7.54eV. At the end of the column, the band gap becomes zero or even negative. It is considered the negative band gap as defined based on the electronic band structure. For CdO, the conduction band minimum is lower than the valence band maximum as obtained within the LDA, so it is called negative band gap. In these calculations, the compounds that have negative band gap are CdO, Tl_2O_3, SnO(36) and PbO_2(136). As it was stated in the previous part, the LDA calculation provides lower value than the experimental results, so as in the case of CdO, all these compounds are still possible for further consideration. In general, it can be concluded that the band gap decreases down the column, i.e. as the cations' period increases, SiO_2 (6.64eV), GeO_2 (3.16eV), SnO_2 (1.76eV), PbO_2 (0.02eV). The band gap increases along the row, i.e. as the cation's valence increases, ZnO (0.8eV), Ga_2O_3

(2.29eV), GeO_2 (3.16eV), AsO_2 (3.47eV).By comparing different phases for the same metal oxides, it can be seen that how the band gap value is related to the symmetry of the crystal structure. Generally, a higher symmetry phase leads to a larger band gap. This can be seen from the case of ZnO, which has a larger band gap in the cubic phase with space group 225 (1.12eV) than in the wurtzite structure 186 (0.8eV). This also can be seen in HgO and SnO. In our calculations, there are also some metal oxides that do not follow the relationship as expected, such as GeO_2. At this point, it still needs to analyze other factors which may affect these calculations.

3.6.2. Electron Effective Mass. LDA calculated electron effective mass is listed in Figure 3.9. For most of the results, it follows from the k*p theory, i.e., the wider the band gap, the larger the effective mass.

From this point of view, it infers that, in general, the electron effective mass is increasing along the cation's row period and decreasing down the cation's column period.

BeO, MgO, CaO, and SrO follow this theoretical trend. Also, the changes of electron effective mass for ZnO (Wurtzite):$0.25m_e$, ZnO (Rocksalt): $0.37m_e$; PbO_2 (136): $0.74m_e$, PbO_2 (225): $0.95m_e$ can be seen. The higher symmetry also provides larger electron effective mass similar to that was mentioned in the band gap part. However, the coordination and the distortions in the cation-anion chains may also affect the electron effective mass, as it has discussed for α-Ga_2O_3 and β-Ga_2O_3, so further investigation based on the partial density of states and crystal structure is needed.

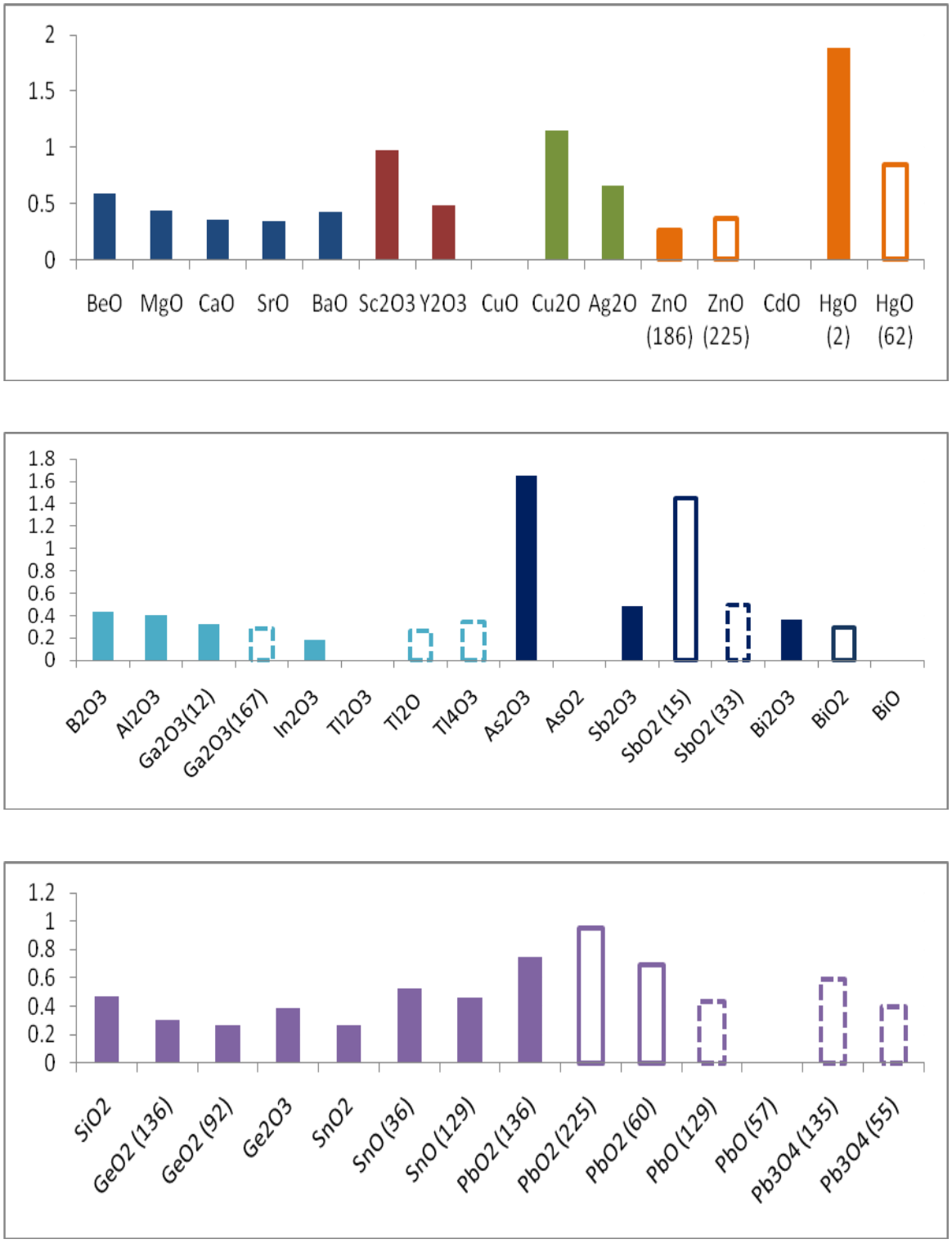

Figure 3.9 Electron effective mass of main group metal oxides

3.7. SUMMARY

By calculating the properties related to the electron band structure, this work aimed to find the most promising TC candidates. In search for novel n-type transparent conductors, electronic band structure calculations for the compounds with same-group next-period cations were performed. First, the electronic band structures were calculated for a number of potential materials. LDA-calculated band gap for the same group metal oxides was compared. The band gap decreases down the column, i.e.as the cations' period increases, .Al_2O_3 (6.45eV), Ga_2O_3 (2.29eV), In_2O_3 (0.96eV), Tl_2O_3 (negative gap); generally, the higher symmetry phase leads to a larger band gap. The band gap increases along the row, i.e., as the cation's valence increases, ZnO (0.8eV), Ga_2O_3 (2.29eV), GeO_2 (3.16eV), AsO_2 (3.47eV). The calculated electron effective mass decreases down the column, i.e. as the cations' period increases. For higher symmetry phases, the effective mass is larger, the series, ZnO (Wurtzite):0.25m_e, ZnO (Rocksalt): 0.37m_e; PbO_2 (136): 0.74m_e, PbO_2 (225): 0.95m_e. For potential TCO candidates, a small effective mass should lead to high carrier mobility in degenerately doped materials.

These results suggest the possibility of predicting the potential transparent conductor candidates by analyzing their electronic properties. Beyond the known TCO hosts, ZnO, In_2O_3, CdO and SnO_2, our results suggest that Ga_2O_3, GeO_2, Bi_2O_3, Sb_2O_3, Tl_4O_3, PbO and Pb_3O_4 might prove promising as TC candidates. Further work is needed to investigate the materials which have been identified based on this work.

4. STUDY ON COMPOUNDS BEYOND OXIDES

4.1. INTRODUCTION

As one of the current well known TCOs, ZnO has many industrial applications owing to its piezoelectric properties and band gap in the near ultraviolet and it has gained substantial interest in the research community in past decades. [88] ZnO is not new to the semiconductor field and the renewed interest is fueled by availability of high-quality substrates and reports of *p*-type conduction when doped with transition metals. In 1975, ZnO/ZnSe *n*-*p* junctions were attained [89] and ZnX (X= O, S, Se and Te) are still expecting to be further explored.

Different from ZnO, CaO exhibits properties typical of an insulator with a wide band gap of 7.7eV and with a dielectric constant of 11.8 [90]. As one of the alkaline-earth oxides, CaO has reduced a great deal of interest for its characteristics such as high mechanical and radiation resistance strengths, transparency in the infrared, visible, and vacuum ultraviolet regions of the spectrum, which open new prospects for its application in various fields. Also, the calcium chalcogenides CaX (X = O, S, Se and Te), together with other alkaline earth chalcogenides form a very important closed shell ionic system at normal conditions. They are technologically important materials, with applications in the area of luminescent devices, an excellent host material for efficient cathode-ray tube phosphors when activated with rare earths, fast high-resolution optically stimulated luminescence imaging and infrared sensitive devices [91–93].

In this section, the compounds of CaX with NaCl structure were studied and the results exhibit a clear trend as the anion's atomic weight increases. The ZnX family materials were also investigated in this work. ZnO, ZnS with wurtzite structure and ZnSe,

ZnTe with zinc blende structure were studied in this work. The crystal structure, electronic band gap, and electron/hole effective mass for these two series of compounds were investigated and will be discussed in detail. The comparison of the two series CaX and ZnX by starting with CaO and ZnO will also be presented.

Besides the materials mentioned above, two other groups of materials were also considered. The first series include Ca_3N_2, Zn_3N_2, AlN, GaN and InN. In the last decade, there is a great activity in the study of the properties of the nitride materials. This interest is due to their possible applications in high power/high temperature electronic and short-wave light emitting devices. Nitride thin films are also of practical use as coating materials because of their higher chemical and thermal stability in various environments and their harder surface [94, 95]. Among the materials listed, GaN was proposed as a candidate for transparent conductive film and has been studied experimentally. [96] This is also the main motivation for the study of this series of compounds. The impurity-doped GaN films are more chemically stable to acid solutions than TCO thin film such as SnO_2, which is one of the criteria for potential TC candidates. In this work, much effort was extended to other nitrides. The set of calculated results by LDA and the comparison of AlN, GaN, and InN will be presented. Also next will go into Ca_3N_2, Zn_3N_2 and GaN, where the cation electronic configuration changes as it moves along the horizontal row in the periodic table.

The last series of compounds presented in this thesis are the fluoride-based group of materials. As it is known so far, most studies of the fluorides are based on the fluoridate glass application and a systematic study to consider these materials as TC candidates has not been reported. In this work, the starting material is CaF_2, ZnF_2, AlF_3,

GaF_3, and InF_3. For the cubic crystal structures used in this study, the electronic band structure and electron/hole effective mass calculations were performed and will be presented in the following discussion. Comparisons will be stated in terms of both horizontal (CaF_2, ZnF_2 and GaF_3) and vertical (AlF_3, GaF_3 and InF_3) variations.

4.2. RESULTS AND DISCUSSION

4.2.1. Crystal Structure. In this part of the work, the crystal structures have been studied include, tetragonal (129, 136), trigonal (167), hexagonal (186), and cubic (206, 216, 225). Four of these crystal structures are listed in Figure 4.1 (shown in space group number), the other structures and the related discussion can be found from the previous section (Figure 3.2). In the next part, it will present the other four (129, 136, 186 and 216) crystal structures.

The CaX series materials share the same crystal structure, which is the rock salt (NaCl) structure discussed in previous chapters. The crystal structure of ZnO and ZnS is wurtzite (space group 186), which is shared with AlN, GaN and InN. A schematic representation of the wurtzite ZnO structure is shown in Figure 4.1. The wurtzite structure has a hexagonal unit cell with two lattice parameters, *a* and *c*, in the ratio of c/a=1.633. The structure is composed of two interpenetrating hexagonal-close-packed (hcp) sublattices, each of which consists of one type of atom displaced with respect to each other along the threefold *c*-axis by the amount of u =3/8=0.375 (in an ideal wurtzite structure) in fractional coordinates (the u parameter is defined as the length of the bond parallel to the *c* axis, in units of *c*). Each sublattice includes four atoms per unit cell and

every atom of one kind (group-II) atom is surrounded by four atoms of the other kind (group VI), or vice versa, which are coordinated at the edges of a tetrahedron.

Tetragonal (129)	Tetragonal (136)
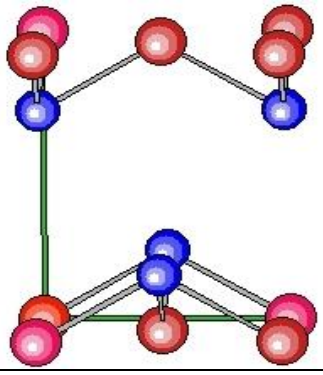	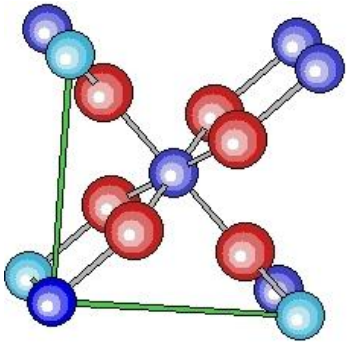
Wurtzite (186)	Cubic (216)
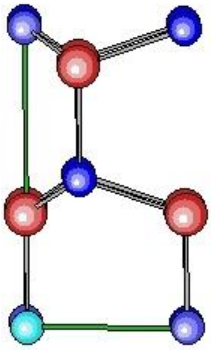	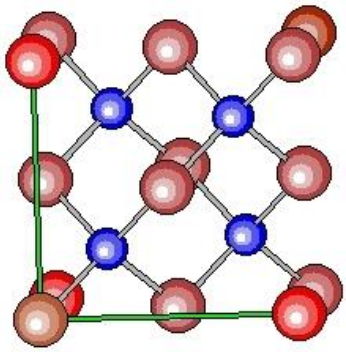

Figure 4.1 Crystal structures of compounds beyond oxides: metal atoms are shown in blue colors and the anion atoms are show in red colors. Anion atom is at the origin.

ZnSe and ZnTe are in zinc blende structure. Zinc blende is based on a face center cubic lattice of anions. The symmetry of the zinc blende structure is given by space group $F\bar{4}3m$ and composed of two interpenetrating face-centered-cubic (fcc) sublattices shifted

along the body diagonal by one-quarter of a body diagonal. There are four atoms per unit cell and every atom of one type (group II) is tetrahedrally coordinated with four atoms of the other type (group VI), and vice versa. Because of the tetrahedral coordination of wurtzite and zinc-blende structures, the four nearest neighbors and 12 next-nearest neighbors have the same bond distance in both structures. In both structures, the cations occupy one of the two types of tetrahedral holes present. In either structure, the nearest neighbor connections are similar, but the distances and angles to further neighbors differ. Zinc blende has 4 asymmetric units in its unit cell whereas wurtzite has 2. Zinc blende is best thought of as a face-centered cubic array of anions cations occupying one half of the tetrahedral holes. Each ion is 4-coordinated and has local tetrahedral geometry.

The crystal structure of space group of 136 for ZnF_2 is also included in the table above, which is from our calculation for PbO_2. Rutile has a primitive tetragonal unit cell, with unit cell parameters a=4.584Å, and c=2.953Å. [97] The metal cations have a coordination number of 6 meaning they are surrounded by an octahedron of 6 oxygen atoms. The oxygen anions have a coordination number of 3 resulting in a trigonal planar coordination. Rutile also shows a screw axis when its octahedra are viewed sequentially.[98] The last crystal structure will be talked about is the one has been calculated for AlF_3, which is a simple tetragonal structure.

4.2.2. Systematic Study of ZnX and CaX (X=O, S, Se, Te). In this section, the results of ZnX and CaX will be discussed and the comparison between these two series will be also presented.

4.2.2.1 ZnX compounds series. The study of ZnX (X=O, S, Se, Te) also started with the electronic band structure. The calculated band gap is shown in Table 4.1. The

electronic band structures of the zinc monochalcogenides calculated by DFT within LDA are shown in Figure 4.2. As it is mentioned above, ZnO and ZnS share the same Wurtzite crystal structure; ZnSe and ZnTe share the same Zinc-blende structure. It is seen from Figure 4.2 that ZnS (2.05eV) has wider band gap than ZnO (0.8eV), the values of the band gaps can be seen in Table 4.1. Compared to ZnTe (0.94eV), ZnSe (1,04eV) has a wider band gap. All the band gaps are direct gap at the Γ point. Apparently, there is no straight trend among this series of materials, which may be due to different crystal structures (hexagonal and cubic). As noted in previous section, the band gaps of ZnX calculated by DFT within the LDA are underestimated compared to the experimental values. The band dispersions come out generally correct.

Table 4.1 Calculated band gap of ZnX and CaX by LDA

Com	Space #	Gap	Com	Space #	Gap
ZnO	186	0.80eV	CaO	225	3.56eV
ZnS	186	2.05eV	CaS	225	2.01eV
ZnSe	216	1.09eV	CaSe	225	1.74eV
ZnTe	216	0.94eV	CaTe	225	1.25eV

It is seen from Figure 4.2 that the conduction band minima (CBM) for ZnX are much more disperse than the valence band maxima (VBM), which shows that holes are much heavier than conduction band electrons in agreement with our findings of effective masses in Table 4.2. Consequently, one can expect that the mobility of electrons is higher than that of holes.

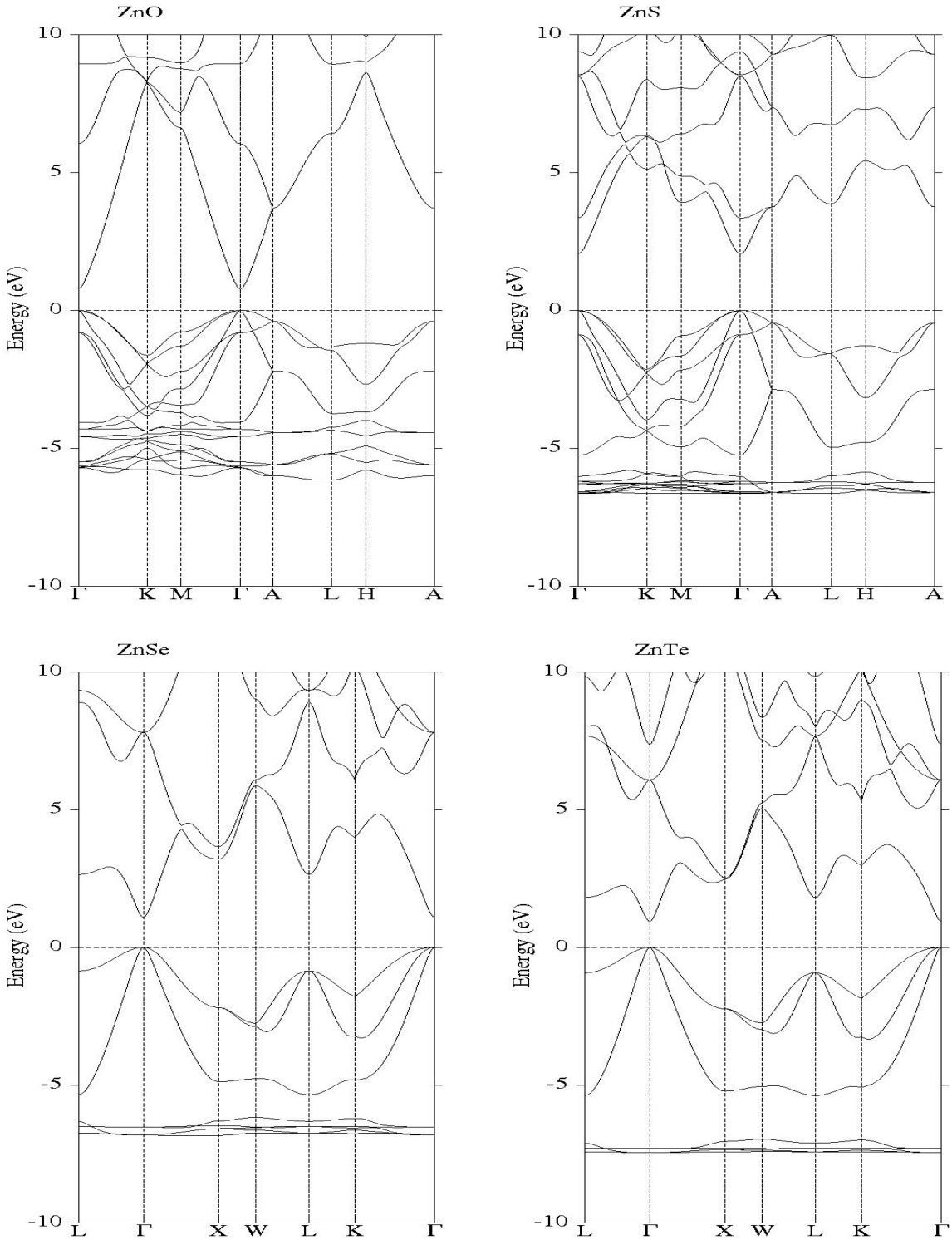

Figure 4.2 Band structures of ZnX: ZnO, ZnS, ZnSe and ZnTe

In Figure 4.3, the density of states of ZnX is shown. It is seen that the results obtained for these ZnX compounds have close similarity, so the partial density of states for ZnO can be took as representative of the others. From the partial density of states of ZnO shown in the Figure 4.4, it can be seen that the zinc *d* states and oxygen *p* state mainly form the VBM.

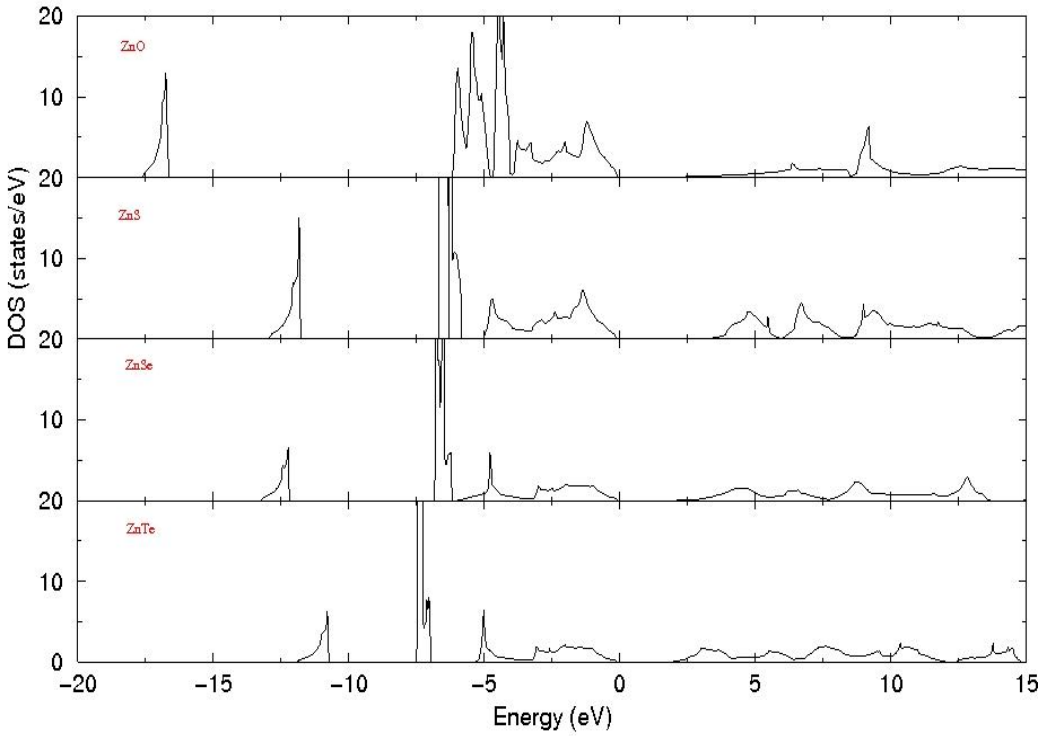

Figure 4.3 Density of states of ZnX: ZnO, ZnS, ZnSe and ZnTe

So, because of the heavy hole effective mass, the contribution of holes to the conductivity is expected to be smaller than that of conduction band electrons even though the concentration of the latter is smaller than the former, which can also been seen from

the partial density of states (Figure 4.4). All these features emphasize the predominant ionic nature of the chemical bonding. Another feature that can be seen from the band structure is that the valence maximum becomes more dispersive with increasing atomic number X, from O to Te.

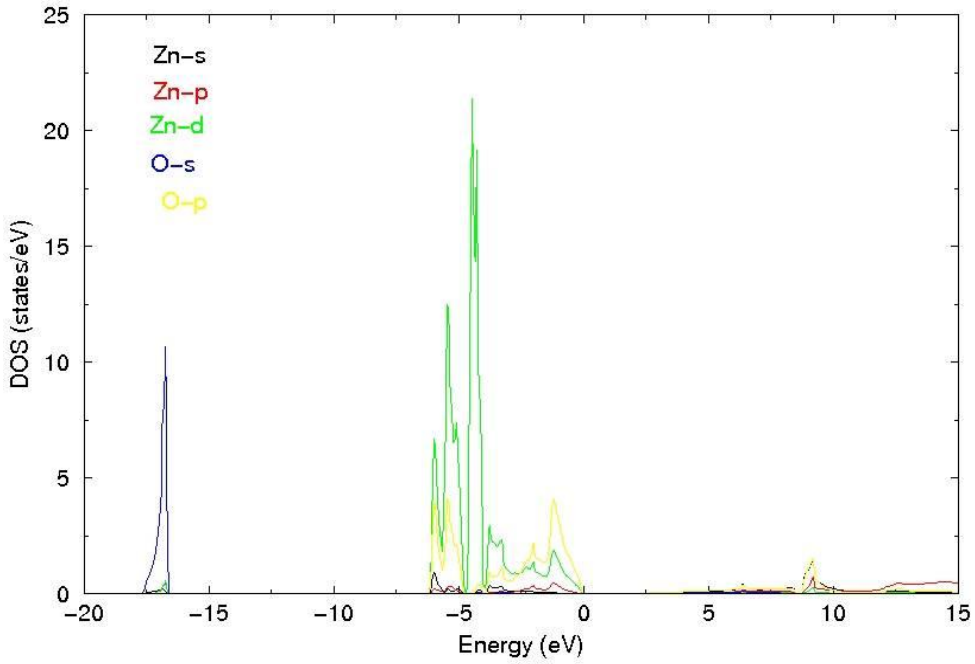

Figure 4.4 Partial density of states of ZnO

From the calculated electron effective mass shown in Table 4.2, it is noticeable that all of the compounds of ZnX series compound have small electron effective mass. All the values are similar and even smaller than conventional TCOs. ZnS, ZnSe, and ZnTe, also possess wide band gaps, which are 2.05eV, 1.09eV and 0.94eV, respectively. Due to the underestimation of the LDA calculation, ZnS, ZnSe, and ZnTe should have a wider band gap than our calculated results. Further accurate calculations can be carried out with this expectation. Within the same crystal structure, as the band gap increases, the

electron effective mass of ZnO and ZnS also increases. This trend is not found for ZnSe and ZnTe.

Table 4.2 Calculated effective mass of ZnX. The effective mass is in units of the electron mass, calculated along the specified crystallographic directions.

Com	Space #	$m_e^{[100]}$	$m_e^{[010]}$	$m_e^{[001]}$	$m_h^{[100]}$	$m_h^{[010]}$	$m_h^{[001]}$
ZnO	186	0.2597	0.2597	0.1936	2.7146	2.7146	3.2751
ZnS	186	0.2621	0.2621	0.1876	1.5921	1.5921	1.6951
ZnSe	216	0.1462	0.1462	0.1462	0.5376	0.5376	0.5376
ZnTe	216	0.2256	0.2256	0.2256	1.2476	1.2476	1.2476

4.2.2.2 CaX compounds series. From Figure 4.5, it is clearly seen that the series of compounds CaX have similar electronic band structures.

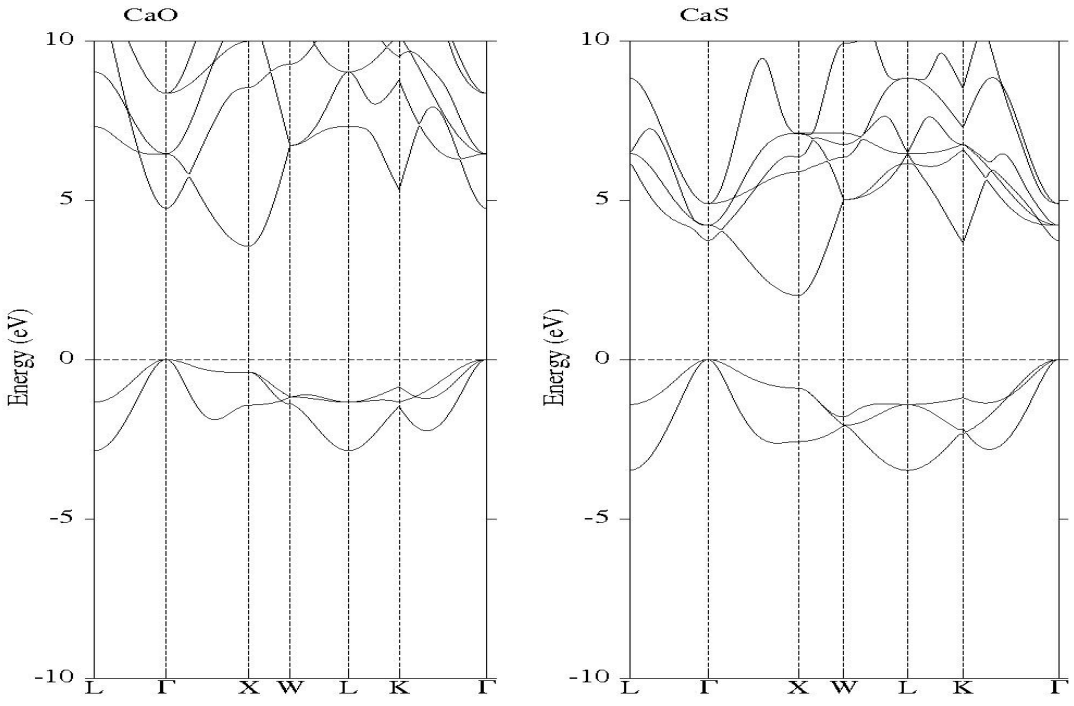

Figure 4.5 Band structures of CaX: CaO, CaS, CaSe and CaTe

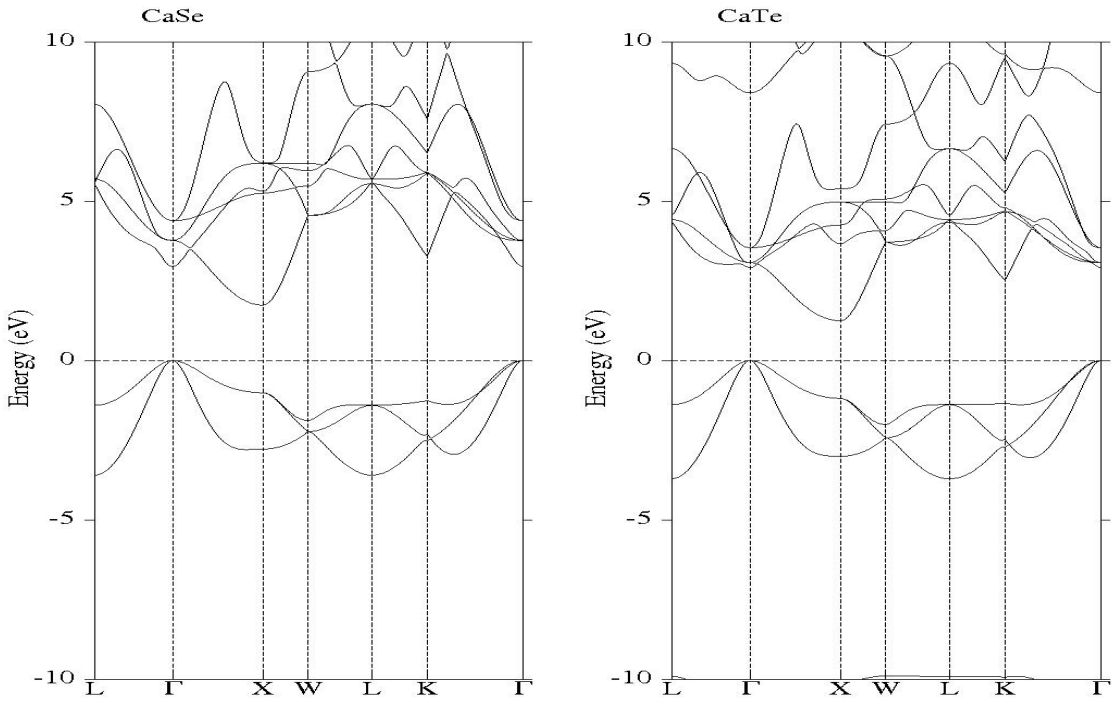

Figure 4.5 Band structures of CaX: CaO, CaS, CaSe and CaTe (cont.)

All of these materials have an indirect band gap between the conduction band minimum at the X point and the valence band maximum at the Γ point. The gap values calculated by LDA are listed in Table 4.1. The band gap values decrease with increasing size of chalcogen atom. This is similar to the vertical groups of compounds discussed in previous section.

The density of states shown in Figure 4.6 corresponds well to the band structure. The low energy side of the density of states consists of a broader structure centered at around -3eV for CaX. This structure originates from chalcogen *s* states, which can be seen from the partial density of states for CaO.

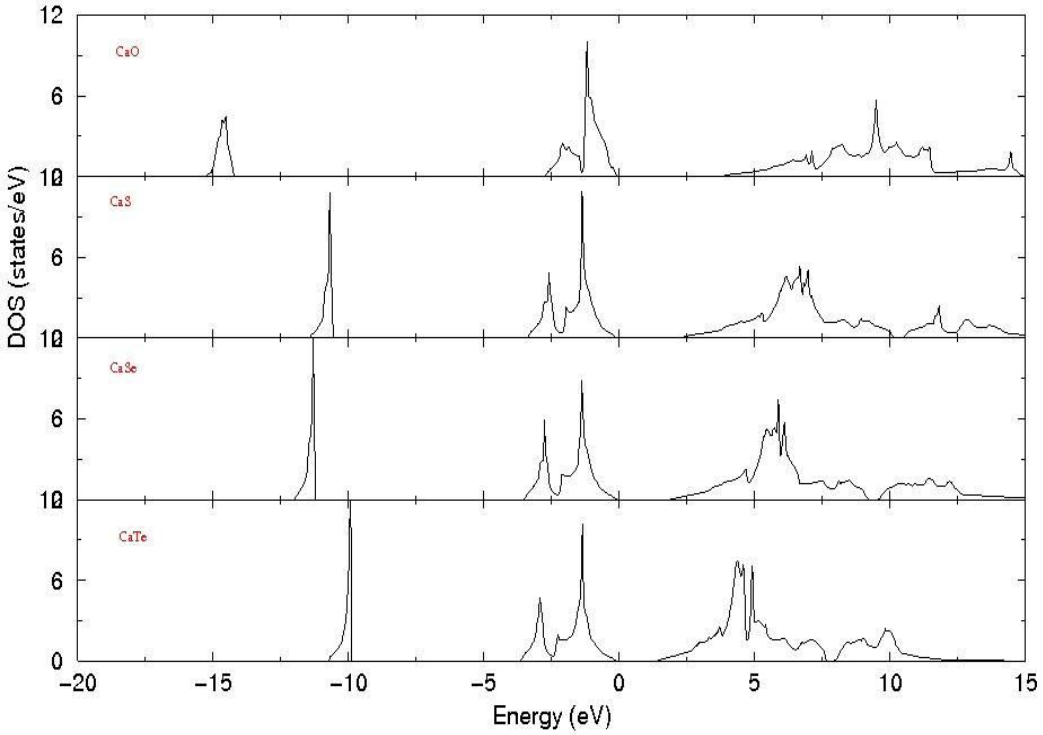

Figure 4.6 Density of states of CaX: CaO, CaS, CaSe and CaTe

Due to the close similarity between the results obtained for these CaX compounds, the partial density of states are given only for CaO in Figure 4.7. The first structure corresponds to the first three overlapping bands in the band structures. It can be seen from the partial density of states that the bands are dominated by the chalcogen *p* states. Also from the partial density of states, the minimum of the conduction band consists mostly of Ca 3*d* states together with very small contributions from chalcogen *p* and *d* states. In marked contrast to ZnO, it is clear that, in the CaO conduction band, the calcium *d* band mainly contributes to the electron distribution. There is no network of metal states with oxygen states as in ZnO. This reveals that the fundamental differences in the electronic properties of these materials originate from the different energy location of the metal's empty *p* and *d* states with respect to the conduction band minimum.

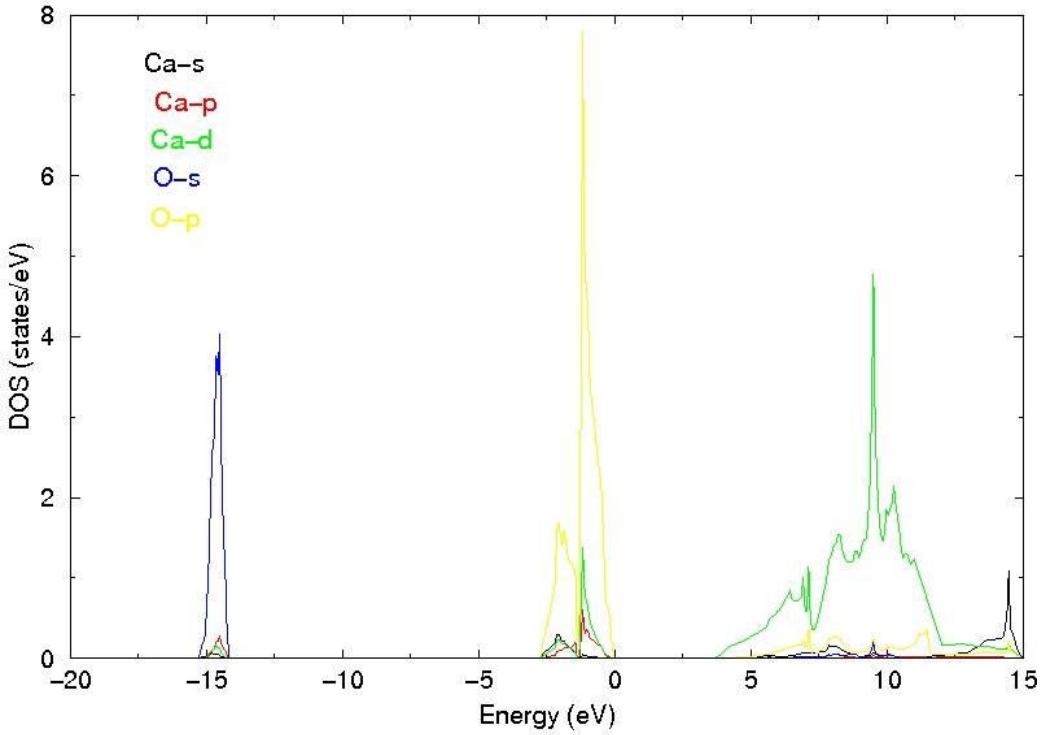

Figure 4.7 Partial density of states of CaO

The calculated electron and hole effective mass are shown in Table 4.3. There have been some reports regarding the electronic band structure [99,100] of this series of materials, however, there are few results on the electron effective mass. Among this series, CaSe results in a smaller electron effective mass, which is $0.2719m_e$, close to the electron effective mass of conventional TCOs.

Table 4.3 Calculated effective mass of CaX. The effective mass is in units of the electron mass, calculated along the specified crystallographic directions.

Com	Space #	$m_e^{[100]}$	$m_e^{[010]}$	$m_e^{[001]}$	$m_h^{[100]}$	$m_h^{[010]}$	$m_h^{[001]}$
CaO	225	0.359	0.359	0.359	2.7436	2.7436	2.7436
CaS	225	0.6059	0.6059	0.6059	0.8588	0.8588	0.8588
CaSe	225	0.2719	0.2719	0.2719	0.7806	0.7806	0.7806
CaTe	225	0.9524	0.9524	0.9524	3.3257	3.3257	3.3257

4.2.3. Nitrides and Fluorides. In this part the nitrides and fluorides discussions about selected nitrides and fluorides are carried out. The electronic band structure, electron effective mass and partial density of states will be presented.

4.2.3.1 Electronic band structure and carrier effective mass of MN. Here M=Al, Ga and In. The band structures of AlN, GaN, and InN are listed in Figure 4.8. All of these three compounds have direct band gap at symmetry point Γ.

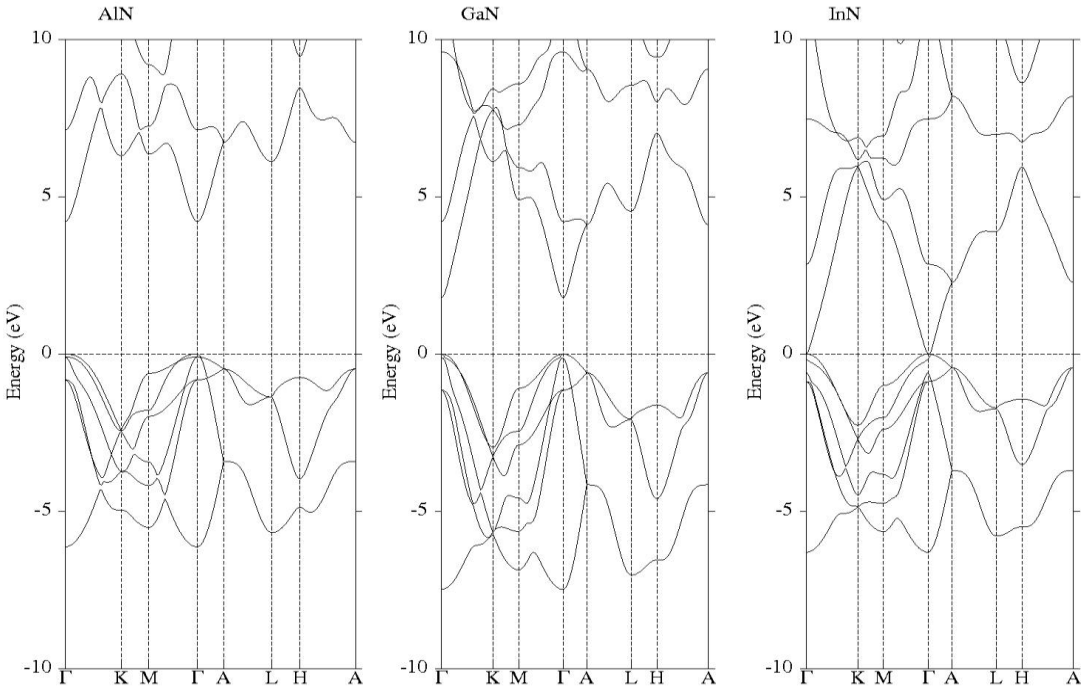

Figure 4.8 Band structures of AlN, GaN and InN

For GaN, the new reported transparent conductor, the band gap is 1.66eV (Table 4.4), according to the LDA calculation. From AlN to InN, the band gap decreases. The band gap value of InN is 0eV, which means that at symmetry point Γ, there is overlap between the conduction band minimum and valence band maximum. According to the underestimation of LDA calculation, InN has a wider band gap than 0eV. According to

the reported related experiment works, the band gap value of InN is still in debate, the scale is 0.5eV~1.4eV. [101,102]

In Figure 4.9, the partial density of states of these three compounds is listed. It is clear to see that at the lowest energy, there is a big contribution from metal *d* states for GaN and InN, which is different from AlN.

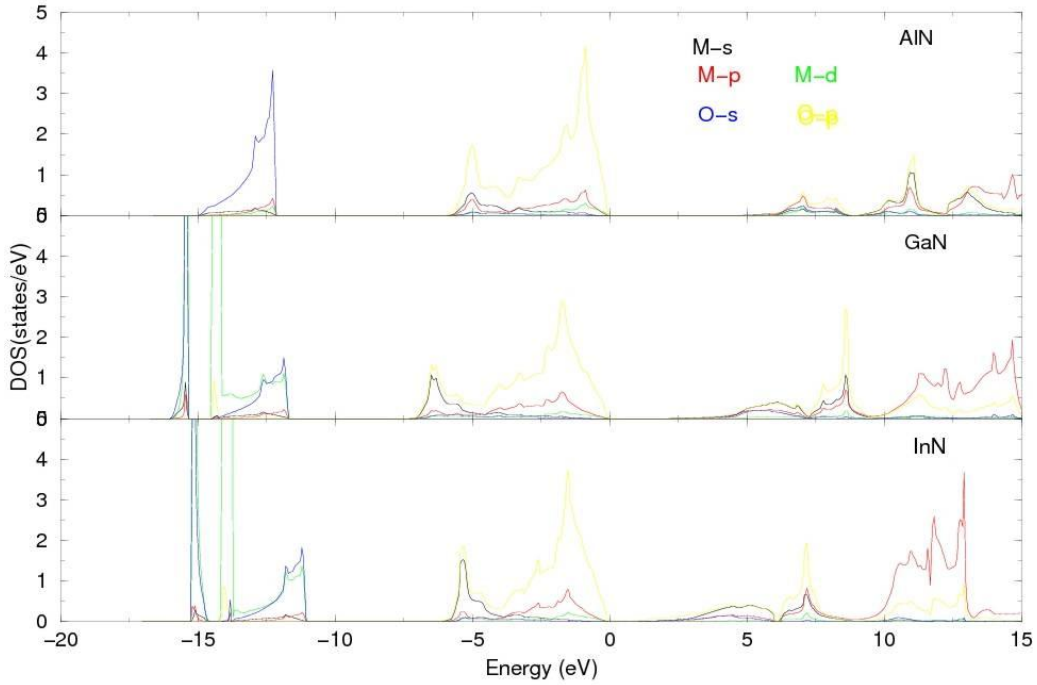

Figure 4.9 Partial density of states of AlN, GaN and InN

The second peaks in the lower energy region are all the same for these compounds. In the conduction band, for AlN, the metal *p* states, metal s states and nitrogen *p* states almost coincide. In GaN and InN, the peak of the metal *p* states is separate from the combined peak of the metal *s* states and nitrogen *p* states, similar to conventional TCOs.

The calculated effective mass is shown in Table 4.5. The electron effective mass is smaller than the hole effective mass as expected, which can be seen from the electronic band structure that the dispersion of the valence band maximum is much flatter than the conduction band minimum. For InN, the band gap is too small to be a candidate like GaN.

4.2.3.2 Analysis of selected nitrides and fluorides. Table 4.4 and Table 4.5 provide the calculated band gap and effective mass for selected nitrides and fluorides and the results of selected oxides from previous sections are also included.

Table 4.4 Calculated band gap of selected nitrides and fluorides

Com	Space #	Gap	Com	Space #	Gap	Com	Space #	Gap
AlN	186	4.21eV	Al_2O_3	167	6.45eV	AlF_3	129	5.01eV
GaN	186	1.66eV	Ga_2O_3	12	2.29eV	GaF_3	167	3.13eV
InN	186	0eV	In_2O_3	206	0.96eV	InF_3	167	2.54eV
Ca_3N_2	206	1.58eV	CaO	225	3.56eV	CaF_2	225	7.03eV
Zn_3N_2	206	0.06eV	ZnO	186	0.80eV	ZnF_2	136	3.69eV

Some trends can be seen in Table 4.4. For the metal elements which are in the same column with the same anion, the band gap decreases down the column, like AlF_3 > GaF_3 > InF_3. For the same cation, the band gap increases as the anion atomic number increases, for example, InN < In_2O_3 < InF_3. For the metal elements in the same row with the same anion, along the row, the band gap is decreasing, like CaF_2 > ZnF_2 > GaF_3. It is noticeable that AlN, Al_2O_3, AlF_3, and CaO, Ga_2O_3, and ZnO do not follow these trends above. These “special” cases indicate that the band gap is also determined by crystal structure as discussed in previous section.

Table 4.5 lists the calculated effective mass for the nitrides and fluorides covered in this study. There are no certain trends that emerge from these results. However, the calculated electron effective mass and band gap of Ca_3N_2 are close to GaN, which can be further investigated in future work using more accurate methods.

Table 4.5 Calculated effective mass for selected nitrides and fluorides

Com	Space #	$m_e^{[100]}$	$m_e^{[010]}$	$m_e^{[001]}$	$m_h^{[100]}$	$m_h^{[010]}$	$m_h^{[001]}$
AlN	186	0.3436	0.3436	0.2986	3.5848	3.5848	1.4653
GaN	186	0.3513	0.3517	0.2162	1.98	1.9804	1.9936
InN	186	0.9524	0.9524	0.2165	2.0241	2.0241	2.1335
Ca_3N_2	206	0.302	0.302	0.302	5.4583	5.4583	5.4583
Zn_3N_2	206	0.0941	0.0941	0.2278	1.1891	1.1891	0.4659

Com	Space #	$m_e^{[100]}$	$m_e^{[010]}$	$m_e^{[001]}$	$m_h^{[100]}$	$m_h^{[010]}$	$m_h^{[001]}$
AlF_3	129	0.467	0.467	0.4944	3.9631	3.9631	9.4867
GaF_3	167	0.5119	0.5119	0.4092	67.4678	67.4678	2.8563
InF_3	167	0.5046	0.5046	0.4298	2.2773	2.2773	1.0312
CaF_2	225	0.5712	0.5712	0.5712	2.7346	2.7346	2.7346
ZnF_2	136	2.2131	2.2131	1.3656	7.031	7.031	0.9436

4.3. SUMMARY

In this section, the electronic band structure, band gap, electron effective mass and hole effective mass were presented for monochalcogenides, nitrides and fluorides.

In the monochalcogenides, the chemical trend was found in CaX, was that as the atomic number of the chalcogen increases, the band gap decreases. Comparison of ZnO and CaO showed that a network of metal *s* states and oxygen *p* states can be found in the ZnO conduction band, with the metal *p* states at higher energy. This is different than in

CaO which the metal *s* and metal *d* states almost coincide. This basic difference between ZnO and CaO is considered the cause of the various electronic property differences in these materials.

Starting with GaN, selected nitrides and fluorides were also discussed. Some chemical trends of band gap were found from the calculated results. The band gap decreases down the cation column and increases along the cation rows, and the band gap increases along the anion's row. Based on the results from this part, two viewpoints from Section 4 were enhanced. First, there are certain trends that can be found for band gap related to the atomic number of anion or cation atomic number only when the crystal structure is the same. The higher symmetry the structure, the wider the band gap is. The other funding is that the effective mass can be predicted from the electronic band structure, although the value is not only proportional to the band gap. Crystal structure and coordination of the cation and anion also play a key role.

In this series of work, ZnS, ZnSe, ZnTe, CaSe, InN, and Ca_3N_2 were highlighted. ZnS, ZnSe, ZnTe, and CaSe all have a small electron effective mass and wide band gap. For InN, the electronic band structure and density of states are similar to GaN. The calculated band gap and electron effective mass of Ca_3N_2 are close to the values of GaN calculated in this work. Based on these results, these compounds can be chosen for future accurate calculation.

5. CONCLUSION

In this research work, first-principles calculation based on DFT theory within the LDA were applied to main group metal oxides, sulfides, selenides, nitrides and fluorides. The electronic band structure, band gap, density of states, electron effective mass, and hole effective mass were then calculated. Comparisons among different categories of compounds were also carried out.

The calculated results reported in Section 3 and Section 4, which are related to conventional TCOs, are in agreement with previous studies and experimental work by others. The results indicate that the network of metal-*s* states and oxygen-*p* states in the conduction band can provide good carrier transport and play a crucial rule in the special properties of TCOs. In the studies within other main group metal oxides, chemical trends of the band gap were found. The band gap is decreasing down the column and increasing along the row. Similar trends are also found in the monochalcogenides, which in increasing the chalcogen atomic number causes the band gap to decrease. By comparing metal nitrides, metal oxides, and metal fluorides, it has been seen that the band gap is increasing from nitrides to fluorides. Also, for some materials, the band gap is determined by the symmetry of their crystal structures. A higher symmetry generally corresponds to a wider band gap. Another point that can be concluded from this study is that the effective mass is not only proportional to the band gap; it also depends on other factors, such as the coordination of the cation and anion. Based on calculated results for the band gap and effective mass, Ga_2O_3, GeO_2, Bi_2O_3, Sb_2O_3, Tl_4O_3, PbO, Pb_3O_4, ZnS, ZnSe, ZnTe, CaS, InN, InF_3, Zn_3N_2 and Ca_3N_2 may prove promising as TC candidates. Further work is

needed to investigate the materials which have been found promising based on these results.

To sum up, systematic comparative electronic band structure investigations not only help to determine the properties of various materials and predict the most promising TC candidates, but also help to formulate general rules on how properties vary with compositions and structures.

BIBLIOGRAPHY

[1] K. Baedeker, *Annalen Der. Physik*., **22**, 749, Leipzig, 1907.

[2] T. Minami, *Semicond. Sci*. **20**, S35, 2005.

[3] K. L. Chopra, S. Major and D.K. Pandya, *Thin Solid Films*, **102**, 1, 1983.

[4] *MRS Bull*. **25**, 2000.

[5] *Transparent Electronics from Synthesis to Apllication*, Wiley, 2010.

[6] T. J. Coutts, J.D. Perkins, D.S. Ginley and T.O. Mason, *195th Meeting of Electrochemical Society*, Seattle, 1999.

[7] D. S. Ginley and C. Bright, *MRS Bull*. **25**, 15, 2000.

[8] R. G. Gordon, Criteria for choosing transparent conductors. *MRS Bull*., **25**, 52–57, 2000.

[9] J. Xue, S. Uchida, B. R. Rand and S. R. Forrest, *Appl. Phys. Lett*. **85**, 5757, 2004.

[10] B. G. Lewis and D. C. Paine, *MRS Bull*. **25**, 22, 2000.

[11] V. D. Mihailetchi, P.W. M. Blom, J. C. Hummelen and M. T. Rispens, Cathode dependence of the open-circuit voltage of polymer: fullerene bulk heterojunction solar cells, *J. Appl. Phys*. **94**, 6849–6851, 2003.

[12] S. J. Pearton, *J. Phys.: Condens. Matter* **16**, R209, 2004.

[13] T. Jansseune, *Compd. Semicond*. **11**, 34, 2005.

[14] T. Jansseune, *Compd. Semicond*. **5**, 33, 2003.

[15] C. A. DiFrancesco, M. W. George, J. F. Carlin Jr., and A. C. Tolcin, "USGS Indium Report," Min. Yearbook, 2007.

[16] C. G. Granqvist, "Applications of Transparent Conductors to Solar Enery," *Transparent Conductors*, 381, 2010.

[17] A. C. Tolcin, "Indium," *U.S.G.S. Min. Commod. Summ*, 2008.

[18] K. W. J. Barnham, M. Mazzer and B. Clive, *Nature Mater*. **5**, 161, 2006

[19] P. Peumans, A. Yakimov and S. R. Forrest, *J. Appl. Phys*. **93**, 3693, 2003.

[20] E. Fortunato, D. Ginley, H. Hosono, and D.C. Paine, *MRS BULLETIN*, **32**, pp. 242-247, March, 2007.

[21] M. Hiramatsu, K. Imaeda, N. Horio, and M. Nawata, *J. Vac. Sci. Technol*., A **16** p.669, 1998.

[22] J. W. Bae, S. W. Lee, and G.Y. Yeom, *J. Electrochem. Soc*. **154**, D34-D37, 2007.

[23] G. J. Exarhos and C. D. Zhou, *Thin Solid Films*, **515**, 7025, 2007.

[24] A. N. Banerjee and K. K. Chattopadhyay, *Progress in Crystal Growth and Characterization of materials*, **50**, 52, 2005.

[25] H. Sato, T. Minami, S. Takata, and T. Yamada, *Thin Solid Films*, **236**, 27, 1993.

[26] H. Kawazoe, *Nature*, **389**, 939, 1997.

[27] J. E. Medvedeva, "Combining Optical Transparency with Electrical Conductivity: Challenges and Prospects," *Transparent Electronics: From Synthesis to Applications, page 1-page 29*, 2010.

[28] E. Burstein, "Anomalous optical absorption limit in InSb," *Phys. Rev.*, **93**, 623-633, 1954.

[29] T. S. Moss, "The interpretation of the properties of indium antimonide," *Proc. Phys. Soc.* B, **67**, 775-782, 1954.

[30] A. J. Freeman, K. R. Poeppelmeier, T. O. Mason, R. P. H. Chang and T. J. "Marks Chemical and thin-film strategies for new transparent conducting oxides," *MRS Bull*., **25**, 45-51, 2000.

[31] O. N. Mryasov and A. J. Freeman, "Electronic band structure of indium tin oxide and criteria for transparent conducing behavior," *Phys. Rev*. B, **64**, 233 111,2001.

[32] R. Asahi, A. Wang, J. R. Babcock, N. L. Edleman, A. W. Metz, M. A. Lane, V. P. Dravid, C. R. Kannewurf, A. J. Freeman and T. J. Marks, "First-principles calculations for understanding high conductivity and optical transparency in $In_xCd_{1-x}O$ films," *Thin Solid Films*, **411**, 101-105, 2004.

[33] H. Mizoguchi and P. M. Woodward, "Electronic structure studies of main group oxides possessing edge-sharing octahedral: implications for the design of transparent conducting oxides," *Chem. Mater.*, **16**, 5233-5248, 2004.

[34] J. E. Medvedeva, "Unconventional approaches to combine optical transparency with electrical conductivity," *Appl. Phys*. A, **89**, 43-47, 2007.

[35] J. E. Medvedeva and A. J. Freeman, "Combining high conductivity with complete optical transparency: a band-structure approach," *Europhys. Lett.*, **69**, 583-587, 2005.

[36] P. P. Edwards, A. Porch, M. O. Jones, D. V. Morgan, and R. M. Perks, *Dalton Trans.* **19**, 2995, 2004.

[37] J. R. Bellingham, W. A. Phillips, C. J. Adkins, *J. Phys. Condens. Mat*., **2**, 1990.

[38] B. Thangaraju, *Thin Solid Films*, **402**, 71, 2002.

[39] G. Frank, H. Kostlin, *Appl. Phys*., A **27**, 197, 1982.

[40] G. Masetti, M. Severi, S. Solmi, *IEEE Trans. Electron Devices*, ED **30**, 764, 1983.

[41] D. Chattopadhyay, H. J. Queisser, *Rev. Mod. Phys*., **53**, 745, 1981.

[42] H. H. Hosono, *J. Non-Cryst. Sol*. **352**, 851, 2006.

[43] C. G. Van de Walle, *Phys. Rev. Lett*., **85**, 1012, 2000.

[44] H. H. Hosono, T. Kamiya, and M. Hirano, Bull. *Chem. Soc. Jpn*. **79**, 1, 2006.

[45] H. Kawazoe, M. Yasukawa, H. Hyodo, M. Kurita, H. Yanagi and H. Hosono, *Nature*, **389**, 939-942, 1997.

[46] A. Kudo, H. Yanagi, H. Hosono and H. Kawazoe, *Appl. Phys. Lett*. **73**, 220-222, 1998.

[47] T. Yamamoto and H. Katayama-Yoshida, Jap. J. of *Appl. Phys. Part 2-Letters*, **38**, 166-169, 1999.

[48] K. Ellmer, J. Phys., D, *Appl. Phys.*, **33**, R17, 2000.

[49] K. Ellmer, J. Phys., D, *Appl. Phys*., **34**, 3097, 2001.

[50] J. Kolink, I.H.Oguzman, K. F. Brennan, R. Wang and P. P. Ruden, *Mat. Res. Soc. Symp. Proc.* Vol. **423**, 1996.

[51] J. M. Seminario (Ed.), "Recent Developments and Applications of Modern DFT," *Elsevier*, Amsterdam, 1996.

[52] K. Schwarz, P. Blaha, G. K. H. Madsen,*Comp.Phys.Commun*.**147**, 71-76, 2002.

[53] P. Hohenberg and W. Kohn, *Phys. Rev*. **136**, B864, 1964.

[54] H. Eschrig, "The Fundamentals of Density Functional Theory," Teubner, Leipzig, 1996.

[55] D. Joulbert (Ed.), "Density Functionals: Theory and Applications," *Springer Lecture Notes in Physics* Vol. **500**, 1998.

[56] C. Fiolhais, F. Nogueira and M. Marques (Eds.), "A Primer in Density Functional Theory," *Springer Lecture Notes in Physics* Vol. **620**, 2003.

[57] R. O. Jones and O. Gunnarsson, *Rev. Mod. Phys*. **61**, 689, 1989.

[58] M. Levy, *Phys. Rev*. A **26**, 1200, 1982.

[59] O. K. Andersen and T. Saha-Dasgupta, *Phys. Rev*. B **62**, 16219, 2000.

[60] E. Zurek, O. Jepsen and O. K. Andersen, *Chem.Phys.Chem*. **6**, 1934, 2005.

[61] E. Wimmer, H. Krakauer, M. Weinert and A. Freeman, *J, Phys. Rev.* B **24** 864, 1981.

[62] W. Koch and M. C. Holthausen, "A Chemist's Guide to Density Functional Theory," *John Wiley & Sons*, New York, 2001.

[63] O. K. Andersen, *Phys.Rev*. B **12**, 3060, 1975.

[64] O. K. Andersen, A.V. Postnikov, and S. Yu. Savrasov, in "Applications of Multiple Scattering Theory to Materials Science," eds. W. H. Butler, P. H. Dederichs, A. Gonis, and R. L. Weaver, *MRS Symposia Proceedings, Materials Research Society*, **253**, 37-70, Pittsburgh, 1992.

[65] O. K. Andersen, O. Jepsen, and D. Glotzel, "Highlights of Condensed-Matter Theory," edited by F. Bassani, F. Fumi, and M. P. Tosi , North-Holland, Amsterdam, 1985.

[66] K. Andersen and O. Jepsen, *Phys. Rev. Lett*. **53**, 2571, 1984.

[67] J. Robertson, *J. Vac. Sci. Technol*. B **18**1, 785, 2000.

[68] F. P. Koffyberg, "Thermoreflectance Spectra of CdO: Band Gaps and Band Population Effects," *Phys. Rev. B*, **13**, 4470–4476, 1976.

[69] Y. Tomm, J. M. Ko, A. Yoshikawa and T. Fukuda, "Floating zone growth of β-Ga_2O_3: a new window material for optoelectronic device applications," *Solar Energy Materials and Solar Cells*, **66**, 1-4, 369-374, 2001.

[70] R. L. Weiher and R. P. Ley, "Optical properties of indium oxide," *J. Appl. Phys*., **37**, 299–302, 1966.

[71] D. Frcohlich, R. Kenklies and R. Helbig, "Band-gap assignment in SnO_2 by two-photon Spectroscopy," *Phys. Rev. Lett*., **41**, 1750–1751, 1978.

[72] J. E. Medvedeva, A. J. Freeman, *Europhys. Lett*. **69,** 583, 2005.

[73] J. Robertson, *J. Phys.* C **12**, 4767, 1979.

[74] R. L. Weiher, R. P. Ley, *J App. Phys*. **37**, 299, 1966.

[75] V. Christou, M. Etchells, O. Renault, P. J. Dobson, O. V. Salata, *J App. Phys.* **88**, 5180, 2000.

[76] V. T. Agekyan, *Phys. Stat. Solidi.* A **43**, 11, 1977.

[77] R. G. Egdell, W. R. Flavell, P. Tavener, *J. Solid State Chem*. **51**, 345, 1984.

[78] R. Ahuja, L. Fast, O. Eriksson, J. M. Wills, and B. Johansson, *J. Appl. Phys.* **83**, 8065, 1998.

[79] R. A. Van Leeuwen, C. J. Hung, D. R. Kammler, and J. A. Switzer, *J. Phys. Chem.* **99**, 15247, 1995.

[80] P. A. Glans, T. Learmonth, K. E. Smith, J. Guo, A. Walsh, G. W. Watson, F. Terzi, and R. G. Egdell, *Phys. Rev.* B **71**, 235109, 2005.

[81] A. Goto, H. Yasuoka, A. Hayashi, and Y. Ueda, *J. Phys. Soc. Jpn*. **61**, 1178, 1992.

[82] V. N. Shukla and G. P. Wirtz, *J. Am. Ceram. Soc*. **60**, 253, 1977.

[83] G. P. Wirtz, C. J. Yu, and R. W. Doser, *J. Am. Ceram. Soc*. **64**, 269, 1981.

[84] V. N. Shukla and G. P. Wirtz, *J. Am. Ceram. Soc*. **60**, 259 1977.

[85] R. J. Phillips, M. J. Shane, and J. A. Switzer, *J. Mater. Res*. **4**, 923, 1989.

[86] H. P. Geserich, *Phys. Status Solidi*. **25**, 74, 1968.

[87] J. E. Medvedeva, E. N. Teasley, M. D. Hoffman, *Phys. Rev.* B, **76**, 155107, 2007.

[88] C. W. Bunn, *Proc. Phys. Soc.* London **47**, 835, 1935.

[89] Tsurkan, *Semiconductors* **6**, 1183, 1975.

[90] M. S. T. Bukowinski, R. Jeanloz, *Geophys. Res. Lett*. **7**, 227, 1980.

[91] Y. Nakanishi, T. Ito, Y. Hatanaka, G. Shimaoka, *Appl. Surf. Sci*. **66**, 515, 1992.

[92] S. Asano, N. Yamashita, Y. Nakao, *Phys. Status Solidi* **89**, 663, 1978.

[93] R. Pandey, S. Sivaraman, *J. Phys. Chem. Solids* **52**, 211, 1991.

[94] J. I. Pankove, J. E. Berkeyheiser, H. P. MarusKa and J. P. Wittke, *Solid State Commun.* **8**, 1051, 1970.

[95] J. I. Pankove, *J. Lumin.* **7**, 114, 1973.

[96] M. A. Khan, J. N. Kuznia, A. R. Bhattarai and D. T. Olsen, *App. Phys. Lett*., **62**, 1786, 1993.

[97] B. Boulard, C. Jacoboni, and M. Pousean, *J. Solid State Chem.*, **80**, 272-276, 1989.

[98] Klein, Cornelis and C. S. Hurlbut, *Manual of Mineralogy*, 20th ed., *John Wiley and Sons*, New York, p. 304-305, 1985.

[99] Z. Charifi, H. Baaziz, F. E. Hassan, N. Bouarissa, *J. Phys. Condens. Mat.* **17**, 4083, 2005.

[100] N. V. Skorodumova, K. Hermansoon, B. Johansson, *Phys. Rev*. B **72**, 125414, 2005.

[101] J. Wu, W. Walukiewicz, K. M. Yu, J. W. Ager III., E. H. Haller, H. Lu, W. J. Schaff, Y. Saito, Y. Nanishi, *Appl. Phys. Lett*. **80**, 3967, 2002.

[102] T. Matsuoka, H. Okamoto, M. Nakao, H. Harima, E. Kurimoto, *Appl. Phys. Lett.* **81**, 1246, 2002.

VITA

Yaou Song was born in Harbin, Heilongjiang, China on October 3rd, 1984. In June 2007, she earned her Bachelor's Degree in Physics from Bejing Jiaotong University, China.